

OPTIMAL CONCEPTUAL DESIGN AND UPGRADE STRATEGIES FOR EVTOL AIRCRAFT UNDER EVOLVING TECHNOLOGIES

Muhammad Alfiyandy Hariansyah[1], Christian Reyner[1], Rhea P. Liem[2] & Pramudita S. Palar[3]

[1]The Hong Kong University of Science and Technology, Clear Water Bay, Hong Kong SAR, 999077
[2]Imperial College London, South Kensington Campus, London SW7 2AZ, United Kingdom
[3]Institut Teknologi Bandung, Bandung, Indonesia, 40132

Abstract

The rapid evolution of energy storage and electric propulsion creates a risk of technological obsolescence for fixed-design electric Vertical Takeoff and Landing (eVTOL) aircraft. This paper introduces a computational framework coupling Multidisciplinary Design Optimization (MDO) with time-dependent technology projections. First, we benchmark Multidisciplinary Feasible (MDF), Individual Discipline Feasible (IDF), and Hybrid MDF–IDF MDO architectures, and select the Hybrid formulation for its overall efficiency, robustness, and optimality in optimizing a Lift-Plus-Cruise eVTOL under varying mission requirements and technology levels. Second, we perform a global sensitivity analysis using variance-based total-order Sobol' indices ($\widehat{S}_T$) on the optimal designs across multiple evaluation years (2030–2070). The results show that optimal designs are governed primarily by battery specific energy ($\widehat{S}_T \approx 0.8 - 1.0$), with powertrain specific powers becoming increasingly influential in later years ($\widehat{S}_T \approx 0.1 - 0.4$), while powertrain efficiencies remain negligible ($\widehat{S}_T \leq 0.1$) due to narrow projection envelopes. Finally, we formulate a discrete upgrade strategy using a future-aware penalty metric, Ψ, based on the required mission energy. Non-uniform upgrade schedules, with early intervals of 5–8 years and later intervals of 10–18 years, consistently outperform uniform 10-year schedules, reducing the excess cumulative energy penalty Ψ by 18.0 % to 22.0 % for clean-sheet redesigns and 1.2 % to 2.9 % for component-swap retrofits. The framework provides a foundation for future-aware eVTOL design under evolving technologies.

Keywords: eVTOL design, MDO, technology projection, sensitivity analysis, upgrade strategy

1. Introduction

The development of electric Vertical Takeoff and Landing (eVTOL) aircraft has gained significant traction in recent years, driven by academic research and industrial investment toward Urban Air Mobility (UAM) [1]. This progress is enabled by the convergence of Distributed Electric Propulsion (DEP), high-density energy storage, and advanced autonomy. DEP distributes multiple smaller electric motors across the airframe [2], exploiting the favorable scaling laws of electric motors, whose power density and efficiency remain comparatively consistent regardless of size [3]. This enables flexible propulsion layouts that can improve control authority [2], lift generation [4], cruise efficiency [5], and

redundancy [6]. In parallel, advances in lithium-ion batteries [7, 8] have made electrically powered aircraft with meaningful payload and range increasingly feasible.

This study focuses on an all-electric architecture, in which a battery system supplies distributed motors through converters to drive the lift rotors and cruise propeller. Prior eVTOL design studies have addressed conceptual sizing [9, 10], large-scale Multidisciplinary Design Optimization (MDO) with coupled aerodynamics, structures, acoustics, and propulsion models [11, 12], battery and thermal modeling [13, 14], configuration comparison [15, 16, 17], component weight scaling [18, 19], design tool assessment [20, 21], trajectory optimization [22, 23, 24], propulsion architecture trade studies [25, 26], and mission-based propeller selection for eVTOL applications [27]. Despite this breadth, a disconnect remains between eVTOL conceptual design optimization and the forecasting of enabling technologies. Many studies still adopt a fixed pack-level battery specific energy, often around $400\,\mathrm{W\,h\,kg^{-1}}$ [11, 17, 26], effectively designing the aircraft for a single technological snapshot rather than a multi-decade lifecycle over which batteries and powertrains are expected to mature.

To represent this evolution, this study adopts published S-curve projections for the three main electric powertrain components. For energy storage, Tiede *et al.* [28] projected pack-level battery specific energy (SE) with substantial uncertainty, with 2026 estimates ranging from $225.5\,\mathrm{W\,h\,kg^{-1}}$ to $446.8\,\mathrm{W\,h\,kg^{-1}}$, as shown in Fig. 1. For electric machines, Pastra *et al.* [29] projected motor specific power to increase from a nominal $10.1\,\mathrm{kW\,kg^{-1}}$ in 2026 to more than $24.3\,\mathrm{kW\,kg^{-1}}$ by 2050, while efficiency remains physically bounded near unity, as depicted in Fig. 2. For converters, Hall *et al.* [30] projected even higher specific powers, with aggressive scenarios exceeding $52.5\,\mathrm{kW\,kg^{-1}}$ by 2050, shown in Fig. 3. These time-dependent envelopes are rarely embedded directly in eVTOL conceptual design optimization, leaving an open question of how evolving technologies reshape optimal vehicle configurations and upgrade schedule/timing decisions.

This paper closes this gap by treating eVTOL conceptual design as a lifecycle decision problem driven by expected technology maturation. It first establishes a sizing and optimization framework for a Lift-Plus-Cruise eVTOL and benchmarks MDO architectures to identify a formulation that is sufficiently efficient and robust for repeated optimization runs. The selected architecture is then used for parameter sweeps and a Sobol' global sensitivity analysis (GSA). The parameter sweeps expose how design objectives and mission requirements shape the optimal aircraft, while the GSA identifies which projected technology variables actually drive the movement of those optima over time. These sensitivity results are used to simplify the lifecycle upgrade problem by retaining only the dominant time-varying technology drivers. The reduced technology vector is then used to construct a *utopian benchmark*, defined here as the ideal year-by-year design trajectory obtained by re-optimizing the aircraft as technology changes, and to formulate a future-aware penalty metric, Ψ, that assesses the proximity of a practical upgrade strategy relative to this continuously re-optimized ideal in terms of cumulative mission energy. Two upgrade modes are considered: clean-sheet redesigns, in which both the airframe design variables and component technologies are updated, and component-swap retrofits, in which the entry-into-service airframe is retained while batteries, motors, and converters are replaced. The main contributions are MDO architecture selection for eVTOL conceptual sizing and optimization, sensitivity analyses of optimal designs under evolving technologies, formulation of the future-aware penalty metric, and upgrade scheduling for redesign and retrofit strategies. Therefore, this study examines not only what an optimal aircraft looks like at a given technology level, but also when its design or components should evolve in response to technology projections.

The remainder is structured as follows. Section 2. establishes the sizing and optimization framework and identifies an efficient MDO architecture. Section 3. studies how optimal designs change with objectives, mission requirements, and technology levels; parameter sweeps reveal design trade-offs, while GSA identifies the dominant technology drivers retained in the subsequent analysis. Section 4. formulates the upgrade strategy using the utopian benchmark and penalty metric Ψ, then compares optimal schedules with uniform schedules. Finally, Section 5. concludes and discusses future work.

https://doi.org/10.71945/icas2026_0631

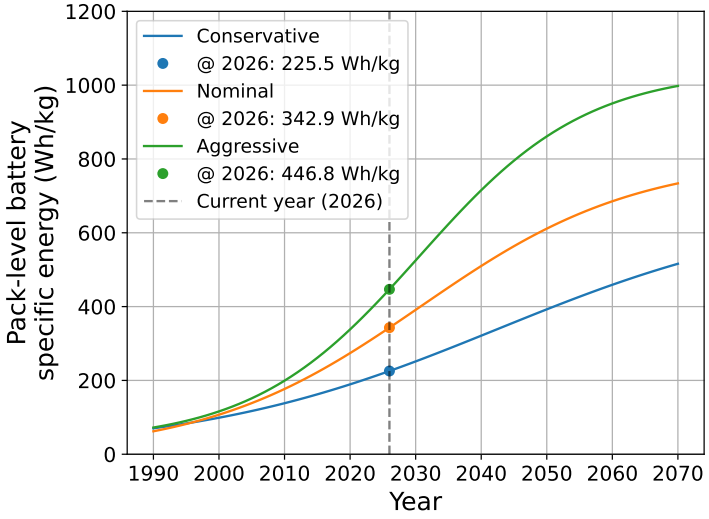
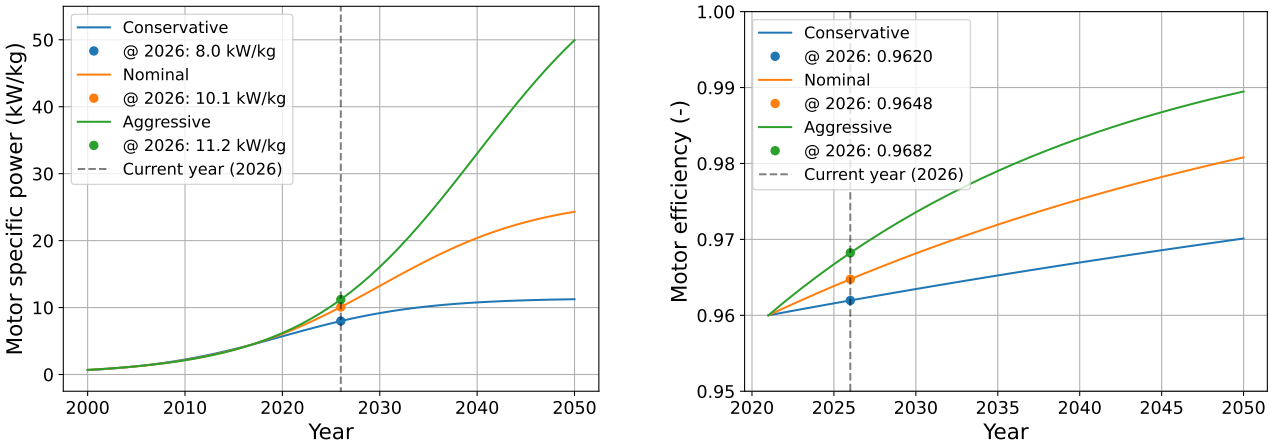
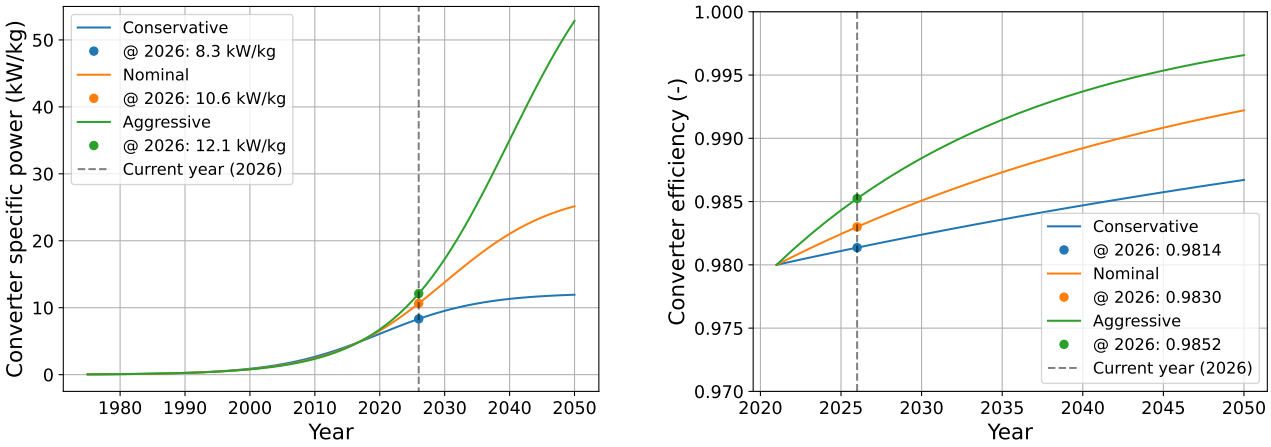


Figure 1 – Pack-level battery specific energy projection based on Tiede *et al.* [28].



(a) Specific Power (b) Efficiency

Figure 2 – Electric motor technology projections based on Pastra *et al.* [29].



(a) Specific Power (b) Efficiency

Figure 3 – Converter technology projections based on Hall *et al.* [30].

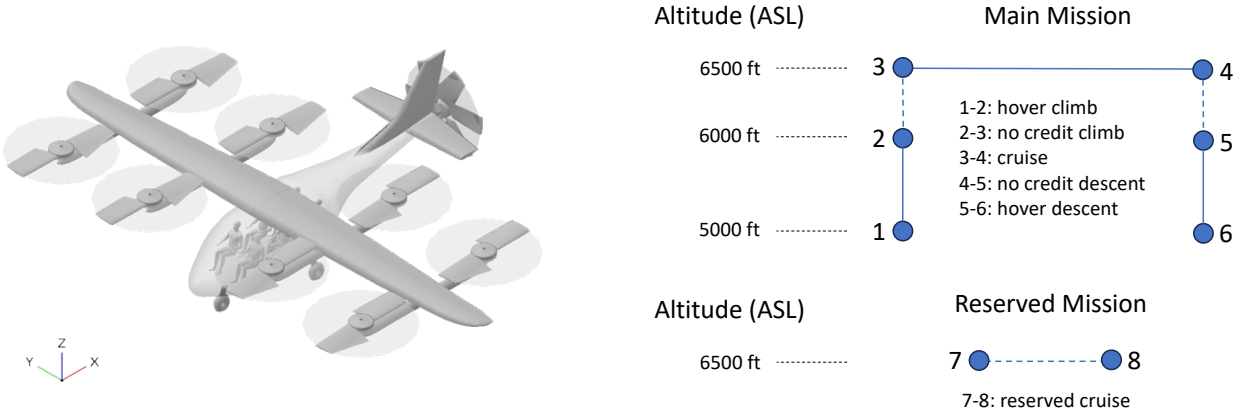
https://doi.org/10.71945/icas2026_0631

2. Conceptual Sizing and Optimization Framework

This section presents the integrated computational framework used to optimize a Lift-Plus-Cruise (LPC) eVTOL aircraft. We define the baseline configuration and mission, detail the multidisciplinary sizing analyses, and formulate the optimization problem within the MDO architecture.

2.1 Baseline Vehicle and Mission

This study utilizes an all-electric LPC eVTOL configuration, adapted from NASA's reference vehicles for UAM [17]. As illustrated in Fig. 4a, this architecture decouples vertical and horizontal flight phases, employing eight distributed rotors mounted on booms for lift and a single tail-mounted pusher propeller for cruise thrust. The aircraft is sized to transport a payload of six passengers (600 kg). The design mission follows the benchmark requirements outlined by Uber Air [31, 32]. The simplified profile, depicted in Fig. 4b, consists of a vertical takeoff from 5000 ft above sea level (ASL) with a constant 500 ft min^{-1} hover climb, a cruise segment at 6500 ft ASL defined by variable range and speed requirements, and a vertical landing with a constant 300 ft min^{-1} hover descent. To comply with Visual Flight Rules (VFR), the energy sizing explicitly accounts for a 20 min reserve cruise segment [33].



(a) NASA LPC OpenVSP Model [34]

(b) Mission Profile

Figure 4 – Baseline LPC eVTOL configuration and the associated design mission profile.

2.2 Multidisciplinary Analyses for Conceptual Sizing

The conceptual sizing process is formulated as a root-finding problem. Given a set of fixed mission parameters ($\mathbf{p}_{\text{mission}}$), vehicle geometric parameters ($\mathbf{p}_{\text{vehicle}}$), payload weight ($W_{\text{payload}}$), design variables ($\mathbf{x}$), and technology levels (Θ), the objective is to find a self-consistent takeoff weight such that the residual weight (W_{residual}) is zero. The $\mathbf{p}_{\text{mission}}$ includes atmospheric conditions (air density, speed of sound, gravitational acceleration) and segment requirements (speed and distance). The $\mathbf{p}_{\text{vehicle}}$ defines fixed geometries such as fuselage length, number of rotors, and empennage areas. The technology vector $\Theta = [\rho_{\text{b}}, \rho_{\text{m}}, \rho_{\text{c}}, \eta_{\text{m}}, \eta_{\text{c}}]$ encapsulates the time-dependent parameter of key components: battery specific energy (ρ_{b}), motor specific power (ρ_{m}), motor efficiency (η_{m}), converter specific power (ρ_{c}), and converter efficiency (η_{c}).

The sizing process is managed by a Multidisciplinary Analysis (MDA) solver utilizing a Newton solver in the OpenMDAO framework [35]. In the XDSM and subsequent MDO formulations, the iterative takeoff-weight value supplied to the disciplinary analyses is denoted by $\widehat{W}_{\text{takeoff}}$. The hat notation indicates an independent copy of the coupling variable, following the coupling-variable-copy convention

commonly used in MDO formulations [36]. This copy is passed to the performance and weight analyses, while the total-weight calculation returns the corresponding updated value W_{takeoff}. The MDA solver then drives the difference between these two quantities to zero through the closure equation:

$$W_{\text{residual}} = h^{\text{c}}(\widehat{W}_{\text{takeoff}}, \mathbf{x}, \Theta, \mathbf{p}_{\text{vehicle}}, \mathbf{p}_{\text{mission}}, W_{\text{payload}}) = \widehat{W}_{\text{takeoff}} - W_{\text{takeoff}} = 0. \tag{1}$$

The sizing procedure is visualized using an eXtended Design Structure Matrix (XDSM) [37] in Fig. 5. The sub-analyses are grouped into two main modules. The *Performance Analysis* module consists of aerodynamics, trim calculation, rotor power, and energy calculation, while the *Weight Analysis* module consists of battery weight, empty weight, and total weight estimation. This grouping is also used in the XDSM diagrams in Section 2.3; for simplicity, Figs. 6–8 show only these two major modules rather than each lower-level sub-analysis. Starting from an initial takeoff-weight copy $\widehat{W}^{(0)}_{\text{takeoff}}$, the MDA solver iterates through these sub-analyses until the residual weight is driven to zero. The two modules are described in the following subsections.

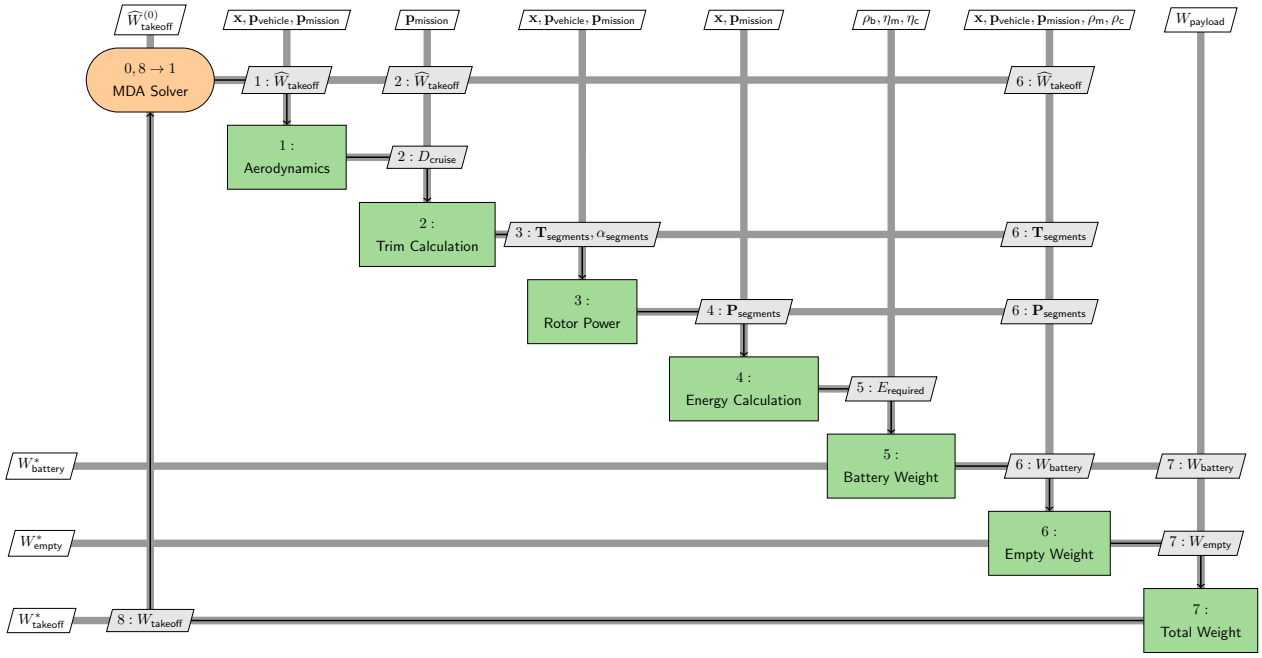


Figure 5 – Detailed XDSM diagram illustrating the sub-analyses for the sizing problem.

2.2.1 Performance Analysis

The performance module consists of aerodynamics, trim calculation, rotor power, and energy calculation. In this framework, airframe aerodynamics are modeled only for forward flight (cruise). The total aerodynamic drag at cruise (D_{cruise}) is calculated as:

$$D_{\text{cruise}} = \frac{1}{2}\rho_{\text{air}} V^2_{\text{cruise}} S_{\text{ref}} \left(C_{D,0} + C_{D,\text{i}}\right), \tag{2}$$

where ρ_{air} is the air density, V_{cruise} is the cruise speed and S_{ref} is the wing reference area, treated here as equivalent to the wing area S_{w}. The parasitic drag coefficient is fixed at $C_{D,0} = 0.0397$. This value is taken from the wind-tunnel measurements of Bacchini *et al.* [38], who reported $C_{D,\min} = 0.0397$ for a QuadPlane model with inactive lift rotors aligned parallel to the freestream. In this paper, this measured minimum drag coefficient is used as a representative cruise parasitic drag coefficient that implicitly accounts for the additional drag of the inactive lift rotor system and supporting structures.

To ensure level flight, the lift L (assumed to be purely produced by the wing) is set equal to the aircraft weight W. The required lift coefficient at cruise ($C_{L,\text{cruise}}$) is therefore calculated as:

$$C_{L,\text{cruise}} = \frac{W}{\frac{1}{2}\rho_{\text{air}} V_{\text{cruise}}^2 S_{\text{ref}}}. \tag{3}$$

The lift-induced drag coefficient ($C_{D,\text{i}}$) assumes a clean-wing parabolic drag polar:

$$C_{D,\text{i}} = \frac{{C_L}^2}{\pi e \mathcal{AR}_{\text{w}}}, \tag{4}$$

where $\mathcal{AR}_{\text{w}}$ is the wing aspect ratio. The Oswald efficiency factor (e), which captures vehicle-level lift-dependent drag, for straight, unswept wings is approximated using Raymer's method [39]:

$$e = 1.78\left(1 - 0.045\,\mathcal{AR}_{\text{w}}^{0.68}\right) - 0.64. \tag{5}$$

To satisfy the vertical force balance during cruise, the angle of attack is obtained from the required lift coefficient. The finite-wing lift-curve slope (a_{w}) is computed using Prandtl lifting-line theory with a compressibility correction [40] applied to the airfoil lift-curve slope (a_0):

$$a_{\text{w}} = \frac{a_0}{\sqrt{1-M^2} + \frac{a_0}{\pi e_{\text{span}} \mathcal{AR}_{\text{w}}}}, \tag{6}$$

where M is the Mach number at cruise and e_{span} is the span efficiency factor used in the finite-wing lift-curve-slope correction. Following Leishman [40], departures from the ideal elliptical spanwise loading can be represented by a factor δ, where

$$e_{\text{span}} = \frac{1}{1+\delta}. \tag{7}$$

For practical plain wings, Leishman indicates that δ typically lies between approximately 0.01 to 0.1, corresponding to $e_{\text{span}} \approx 0.90 - 0.99$. Therefore, $e_{\text{span}} = 0.9$ is adopted here as a conservative value to account for non-elliptic loading and interference effects from the fuselage and propulsion-related structures. The trimmed angle of attack is then

$$\alpha_{\text{trim}} = \frac{(C_L - C_{L,0})}{a_{\text{w}}}. \tag{8}$$

The coefficients $a_0 = 6.512\,\text{rad}^{-1}$ and $C_{L,0} = 0.240$ were obtained from XFOIL runs of the NACA 2412 airfoil at Reynolds number $\text{Re} = 4 \cdot 10^6$ and $M = 0.2$, representative of cruise conditions [32].

Following the trim calculation, the rotor power is analyzed using momentum theory for vertical flight [41, 42, 43] and a modified momentum theory for forward flight [16, 23, 43, 44] to determine the required shaft powers at each segment (P_{seg}). Consequently, the total required mission energy E_{required} is the sum of energy consumed across all mission segments plus a regulatory reserve:

$$E_{\text{required}} = \sum_{\text{seg}} P_{\text{seg}}\, t_{\text{seg}} + E_{\text{reserve}}. \tag{9}$$

The reserve energy (E_{reserve}) satisfies the VFR requirement of 20 min at cruise power [33]. To determine the necessary energy storage, the total system efficiency η_{system} is defined as the product of component efficiencies:

$$\eta_{\text{system}} = \eta_{\text{m}}\, \eta_{\text{c}}\, \eta_{\text{others}}. \tag{10}$$

Here, η_{m} and η_{c} represent the motor and converter efficiencies, respectively. While state-of-the-art (SOA) values are $\eta_{\text{m}} = 0.96$ and $\eta_{\text{c}} = 0.98$, these parameters are treated as variables subject to technology projections [29, 30]. The term η_{others} accounts for non-propulsive losses and is fixed at 0.9. This yields a baseline SOA system efficiency of approximately 0.85, consistent with the typical 80 % to 90 % efficiencies observed in battery electric vehicles using modern lithium-ion technologies [45].

2.2.2 Weight Analysis

The weight module calculates the battery weight, empty weight, and total weight of the aircraft. First, the battery weight is sized to deliver the required energy without exceeding a maximum depth of discharge (DoD_{max}) of 0.8 [46]:

$$W_{\text{battery}} = \frac{E_{\text{required}}}{DoD_{\text{max}}\,\rho_{\text{b}}\,\eta_{\text{system}}}, \tag{11}$$

where ρ_{b} denotes the battery SE (W h kg^{-1}), which is also subject to technology projection [28].

Next, the aircraft empty weight (W_{empty}) is estimated by summing the weights of propulsion, structure, and equipment groups, adjusted by technology factors (tf):

$$W_{\text{empty}} = \text{tf}_{\text{prop}} W_{\text{prop}} + \text{tf}_{\text{struct}} W_{\text{struct}} + \text{tf}_{\text{equip}} W_{\text{equip}}. \tag{12}$$

We apply $\text{tf}_{\text{prop}} = \text{tf}_{\text{struct}} = 1.0$ and $\text{tf}_{\text{equip}} = 0.8$ to account for modern equipment scaling. The component weight models are summarized in Table 1.

For the propulsion sizing, a power margin (PM) of 0.5 is applied to the maximum required shaft power (P_{req} in kW) to ensure redundancy and maneuverability. The weights of the electric motors and converters are derived from their respective specific power capabilities, denoted as ρ_{m} and ρ_{c}. These parameters are subject to technology projections [29, 30], which anticipate performance improvements over time. For the baseline analysis, the SOA values are $\rho_{\text{m}} = 6.0\,\text{kW kg}^{-1}$ and $\rho_{\text{c}} = 7.5\,\text{kW kg}^{-1}$.

The structural weight models are adopted from the large-scale MDO study of Sarojini *et al.* [11], in which regression models were trained from finite-element-based structural sizing data for an LPC configuration. These models estimate fuselage, wing, boom, and empennage weights as functions of wing area, aspect ratio, fuselage length, battery weight, cruise speed, and tail areas. Landing gear and equipment weights are estimated using empirical correlations for helicopters [20, 41, 47].

Finally, the residual weight driving the convergence is calculated as:

$$W_{\text{residual}} = \widehat{W}_{\text{takeoff}} - (W_{\text{payload}} + W_{\text{battery}} + W_{\text{empty}}). \tag{13}$$

Table 1 – Summary of Component Weight Estimation Models

Component	Model / Equation	Reference
Propulsion		
Rotors & Hubs	$N_{\text{rotor}}(0.0095\,T_{\text{req,hover}}/N_{\text{rotor}} - 1.9275) + (0.0095\,T_{\text{req,cruise}} - 1.9275)$	Duffy *et al.* [18]
Motors	$(1+PM)\,P_{\text{req}}/\rho_{\text{m}}$; where ρ_{m} is the motor SP (SOA: 6.0 kW kg^{-1})	Pastra *et al.* [29]
Converters	$(1+PM)\,P_{\text{req}}/\rho_{\text{c}}$; where ρ_{c} is the converter SP (SOA: 7.5 kW kg^{-1})	Hall *et al.* [30]
Structure		
Fuselage	$1.015\,S_{\text{w}} - 0.407\,\mathcal{R}_{\text{w}} + 42.60\,L_{\text{f}} + 0.031\,W_{\text{battery}} + 0.069\,V_{\text{cruise}} - 116.73$	Sarojini *et al.* [11]
Wing	$11.138\,S_{\text{w}} + 31.476\,\mathcal{R}_{\text{w}} + 0.789\,L_{\text{f}} - 0.021\,W_{\text{battery}} + 0.240\,V_{\text{cruise}} - 320.24$	Sarojini *et al.* [11]
Booms	$3.339\,S_{\text{w}} + 5.400\,\mathcal{R}_{\text{w}} - 0.092\,L_{\text{f}} + 1.3\times10^{-4}\,W_{\text{battery}} - 0.006\,V_{\text{cruise}} - 11.70$	Sarojini *et al.* [11]
Empennage	$8.433\,S_{\text{ht}} + 10.054\,S_{\text{vt}} - 0.199$	Sarojini *et al.* [11]
Landing Gear	$0.0325\,W_{\text{takeoff}}$ (wheeled)	Johnson [20]
Equipment		
Avionics	$0.0268\,W_{\text{takeoff}}$	Roskam [47]
Anti-icing	$0.008\,W_{\text{takeoff}}$	Prouty [41]
Flight Controls	$11.5\,(W_{\text{takeoff}}/1000)^{0.4}$ (Imperial units, lb)	Prouty [41]
Furnishings	$13.0\,(W_{\text{takeoff}}/1000)^{1.3}$ (Imperial units, lb)	Prouty [41]

2.3 MDO Architecture: MDF, IDF, and Hybrid MDF–IDF

The sizing MDA in Fig. 5 can be extended into an MDO procedure, allowing the framework not only to converge the takeoff weight for a fixed geometry but also to identify an optimal design variable set, $\mathbf{x}$, for a predefined optimization problem. In this study, three MDO architectures were investigated: Multidisciplinary Feasible (MDF), Individual Discipline Feasible (IDF), and Hybrid MDF–IDF; see Martins and Lambe [36] for a detailed theoretical comparison. These architectures differ primarily in how they treat coupling variables, as illustrated by the corresponding XDSM diagrams in Figs. 6–8.

In the MDF architecture, shown in Fig. 6, the optimizer controls only the design variables, $\mathbf{x}$. At each optimizer evaluation, an inner MDA solver, such as a Newton solver, is used to iteratively converge the coupling variable copy $\widehat{W}_{\text{takeoff}}$. As a result, every design point evaluated by the optimizer corresponds to a fully sized and physically consistent aircraft. By contrast, the IDF architecture, shown in Fig. 7, removes the inner MDA solver and decouples the disciplines so that performance and weight modules can be executed independently. The optimizer controls both the design variables and independent copies of the coupling variables, such as $\widehat{W}_{\text{takeoff}}$, $\widehat{E}_{\text{required}}$, $\widehat{\mathbf{T}}_{\text{segments}}$, and $\widehat{\mathbf{P}}_{\text{segments}}$. Consistency constraints are then imposed to ensure that these optimizer-controlled estimates match the corresponding discipline outputs. The Hybrid MDF–IDF architecture, shown in Fig. 8, provides an intermediate formulation between MDF and IDF. Similar to IDF, it removes the inner MDA solver and allows the optimizer to control $\widehat{W}_{\text{takeoff}}$ directly as a design variable. However, it retains the sequential execution characteristic of the MDF architecture. In this formulation, multidisciplinary consistency is enforced through a single consistency constraint, h^{c}, defined by $W_{\text{residual}} \equiv \widehat{W}_{\text{takeoff}} - W_{\text{takeoff}} = 0$.

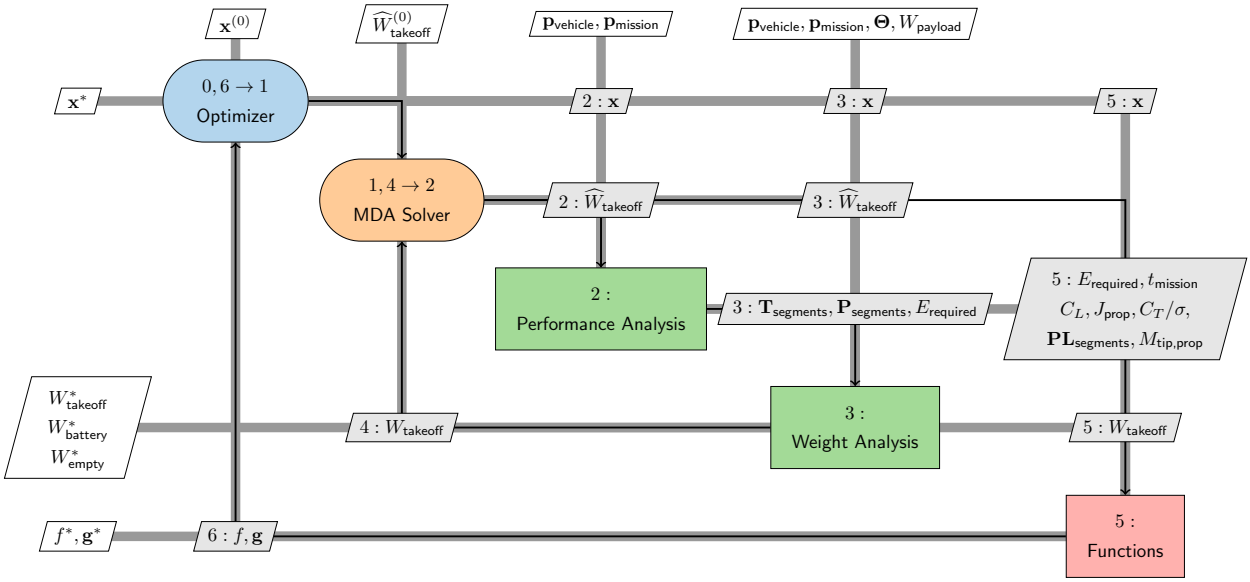


Figure 6 – XDSM diagram of the Multidisciplinary Feasible (MDF) architecture.

To select the most suitable architecture, we performed a comparative benchmark implemented in the OpenMDAO framework [35], utilizing the gradient-based SLSQP optimizer. Because the selected architecture is later used for various sensitivity analyses, it must remain efficient and robust over many repeated optimization problems. Moreover, optimizer performance can depend on the mission requirement, objective function, cruise speed treatment, and initial guess. Therefore, the benchmark was designed to test each architecture over a representative set of optimization conditions. The benchmark considered 550 distinct cases defined by varying mission ranges (10 km to 220 km), objectives (minimizing weight, energy, or time), and cruise speeds (fixed within 220 km h^{-1} to 320 km h^{-1} or treated as a design variable). To assess robustness against local minima, five initial guesses for $\widehat{W}^{(0)}_{\text{takeoff}} \in \{1000, 2000, 3000, 4000, 5000\}$ kg were applied. This resulted in 2750 optimization runs per architecture. The comparison metrics included computational cost, robustness, and solution quality.

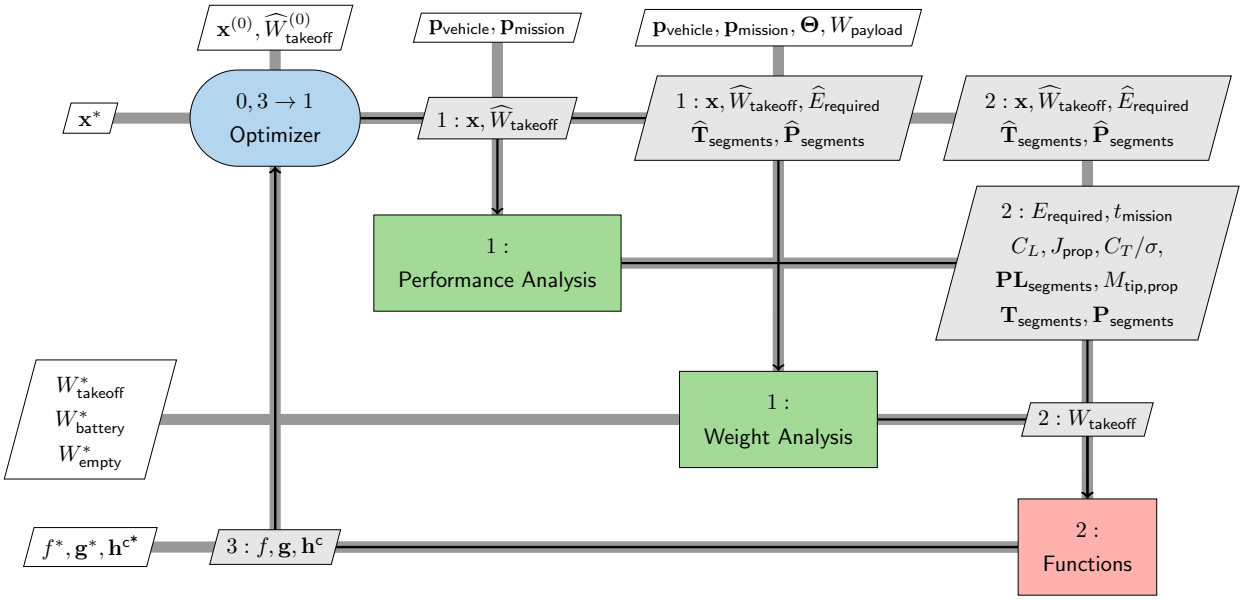


Figure 7 – XDSM diagram of the Individual Discipline Feasible (IDF) architecture.

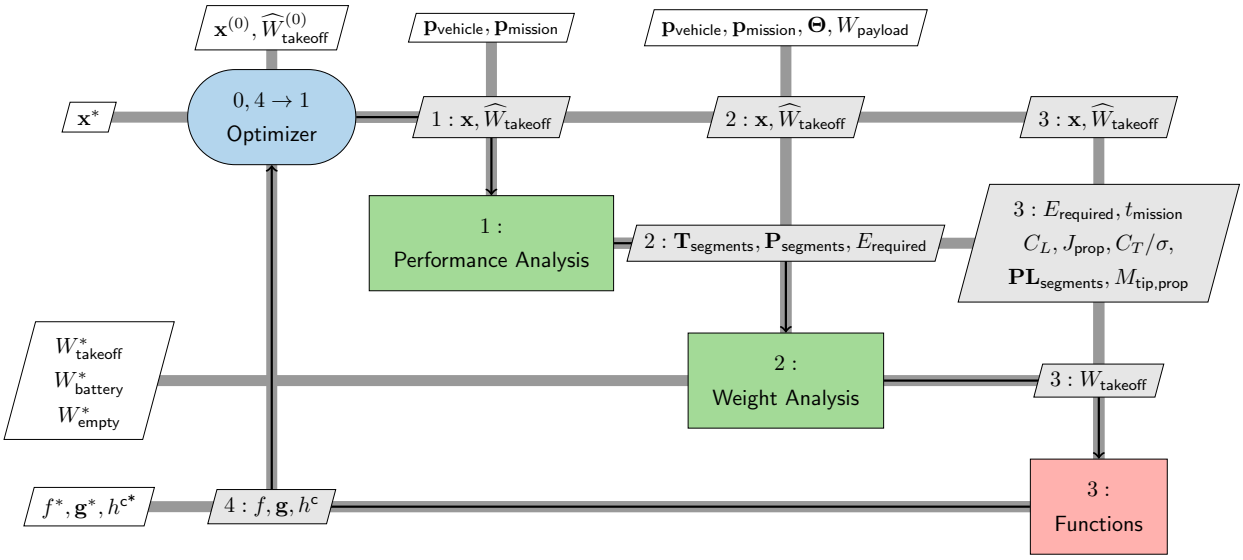


Figure 8 – XDSM diagram of the Hybrid MDF–IDF architecture.

The results are summarized in Table 2. The Hybrid requires the fewest MDA calls, with a mean of 15 compared with 21 for IDF and 282 for MDF. All three architectures achieve 100 % global and case-level success rates, demonstrating their robustness for the current problem. Solution quality was compared across all 550 cases in which they returned feasible designs. For each case, the architecture with the lowest objective value was identified. A case was counted as a *non-tied best* result when one architecture produced a lower objective value than the other two, rather than sharing the best value within numerical precision. Under this criterion, Hybrid produced the non-tied best objective value in 392 cases, MDF in 98 cases, and IDF in 38 cases. The remaining 22 cases were tied best results under the time-minimization case, where they reached the cruise speed upper bound. Based on its lowest computational cost, robustness, and best solution quality, the Hybrid architecture is adopted for the remainder of this study. The parameter sweeps and general sensitivity analysis in Section 3. and the upgrade strategy in Section 4. all rely on repeatedly solving the same optimization problem (with different parameters), which require thousands of optimization runs.

Table 2 – Performance Comparison of MDF, IDF, and Hybrid Architectures

Metric	MDF	IDF	Hybrid
Computational Cost			
Mean MDA Calls (All Runs)	282	21	15
Median MDA Calls (All Runs)	289	21	16
Robustness			
Global Success Rate (All Runs)	100.0 %	100.0 %	100.0 %
Case Success Rate (Multi Start)	100.0 %	100.0 %	100.0 %
Solution Quality (Optimality)			
(Based on 550 cases where the three were feasible)			
Non-tied Best Objective Value	98	38	392
Tied Best Objective Value		22	

2.4 Optimization Problem Formulation

The optimization problem is formulated using the Hybrid MDO described in Section 2.3 and is detailed in Table 3. In this approach, the takeoff weight copy ($\widehat{W}_{\text{takeoff}}$) is treated as a design variable controlled by the optimizer. To ensure physical consistency, an equality constraint is imposed on the residual weight. The optimization problem can be expressed as:

$$\begin{aligned} \underset{\mathbf{x},\widehat{W}_{\text{takeoff}}}{\text{minimize}} \quad & f(\mathbf{x},\widehat{W}_{\text{takeoff}},\Theta) \\ \text{subject to} \quad & h^{\text{c}}(\mathbf{x},\widehat{W}_{\text{takeoff}},\Theta) = W_{\text{residual}} = 0, \\ & \mathbf{g}(\mathbf{x},\widehat{W}_{\text{takeoff}},\Theta) \leq 0, \\ & \mathbf{x}_{\text{lb}} \leq \mathbf{x} \leq \mathbf{x}_{\text{ub}}, \\ & \widehat{W}_{\text{takeoff,lb}} \leq \widehat{W}_{\text{takeoff}} \leq \widehat{W}_{\text{takeoff,ub}}. \end{aligned} \tag{14}$$

Three objectives are considered: minimizing gross takeoff weight, required mission energy, or main mission time. The design variables include wing planform parameters, propulsion geometry, propeller RPM, and cruise speed (unless prescribed by the mission). The constraints enforce residual-weight consistency, cruise lift coefficient, propeller blade loading, power loading, rotor-fuselage clearance, advance ratio, and tip Mach limits. The takeoff-weight lower bound is set by the fixed payload, whereas the upper bound of 5700 kg follows the EASA SC-VTOL-02 MTOW limit [48].

3. Sensitivity Study of Optimal Designs

This section investigates the sensitivity of optimal designs to design objectives, mission requirements, and battery specific energy (SE). Subsequently, it quantifies the impact of technological uncertainties through a global sensitivity analysis based on time-dependent projection envelopes. The results determine which technology trends must be retained in the future-aware upgrade strategy of Section 4., and which variables can be simplified without substantially affecting the conceptual-level conclusions.

3.1 Sensitivity to Design Objectives, Mission Requirements, and Battery Specific Energy

Two parameter-sweep studies were conducted. First, the objectives of minimizing weight, energy, and time were evaluated over mission ranges of 10 km to 220 km and battery SE levels of 250 W h kg^{-1}, 400 W h kg^{-1} and 550 W h kg^{-1}, with cruise speed treated as a design variable. Second, to map feasibility over the mission requirement space, weight-minimization problems were solved over the same range sweep while cruise speed was fixed between 160 km h^{-1} to 320 km h^{-1}.

Table 3 – Optimization problem formulation for the LPC eVTOL configuration.

	Function/Variable	Lower	Upper	Units	Description
Objectives	W_{takeoff}	–	–	kg	Minimize takeoff weight
	E_{required}	–	–	W h	Minimize required energy
	t_{mission}	–	–	s	Minimize mission time
Design Vars.	$\widehat{W}_{\text{takeoff}}$	600.0	5700.0	kg	Takeoff weight copy
	S_{w}	6.0	30.0	m^2	Wing area
	$\mathcal{AR}_{\text{w}}$	4.0	14.0	–	Wing aspect ratio
	r_{rotor}	0.8	2.5	m	Lift rotor radius
	r_{prop}	0.8	2.1	m	Propeller radius
	Ω_{prop}	500.0	2000.0	RPM	Propeller cruise RPM
	V_{cruise}	160.0	320.0	km h^{-1}	Cruise speed
Constraints	W_{residual}	0.0	0.0	kg	Residual weight
	$C_{L,\text{cruise}}$	–	0.6	–	Cruise lift coefficient
	C_T/σ	–	0.14	–	Propeller blade loading
	$\mathbf{PL}_{\text{segments}}$	–	12.0	g W^{-1}	Power loadings
	$\Delta_{\text{clearance}}$	–	0.0	m	Rotor-fuselage interference
	J_{prop}	–	1.3	–	Propeller advance ratio
	$M_{\text{tip,prop}}$	–	0.7	–	Propeller tip Mach

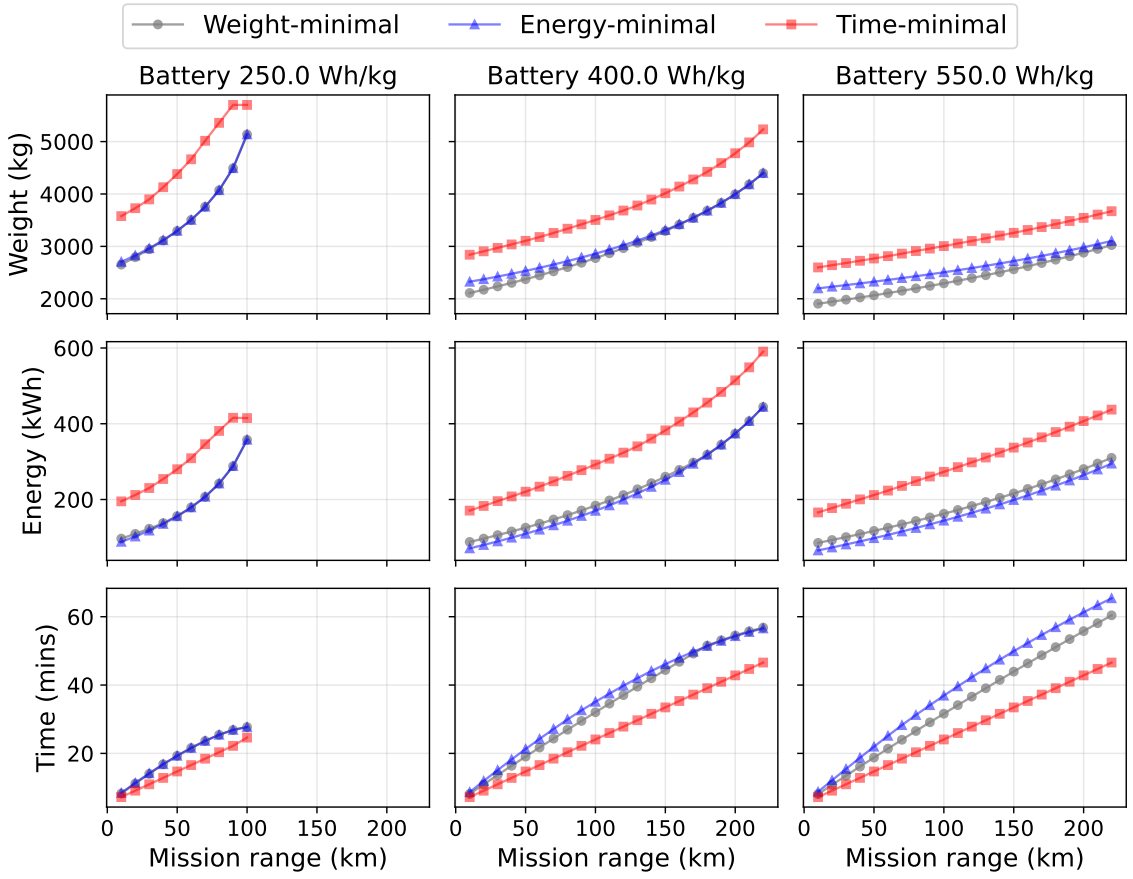


Figure 9 – Comparison of optimal objectives versus mission range under varying battery SE levels.

The results for the first sensitivity study are presented in Fig. 9. As expected, the optimal takeoff weight, required energy, and main mission time increase monotonically with mission range across all objectives. A primary observation is that the trade-offs between weight-minimal (WM) and energy-minimal (EM) designs are closely aligned, evidenced by the nearly overlapping curves. This alignment occurs because reducing takeoff weight inherently lowers the power required for lift, thereby

reducing energy consumption. However, subtle trade-offs persist: WM designs achieve the absolute lowest weight at the cost of slightly higher energy consumption compared to their EM counterparts, and vice versa. Conversely, time-minimal (TM) designs exhibit significantly higher takeoff weights and energy consumption due to the power penalties associated with high-speed flight.

Figure 9 also highlights the critical role of battery SE in determining feasibility. At a battery SE of 250 W h kg^{-1}, the mission becomes infeasible beyond 100 km as the takeoff weight hits the upper bound of 5700 kg (the EASA SC-VTOL-02 limit [48]). However, feasibility extends significantly further for SE levels of 400 W h kg^{-1} and 550 W h kg^{-1}. Notably, the gap between weight-minimal and energy-minimal curves increases with higher battery SE. At lower SE, the battery weight constitutes a dominant fraction of the takeoff weight; thus, minimizing energy (and consequently battery weight) strongly correlates with minimizing total weight. At higher SE, the battery weight fraction decreases, decoupling the objectives: WM designs prioritize reducing empty weight (structure, propulsion, equipment), whereas EM designs prioritize aerodynamic efficiency, leading to distinct optimal solutions.

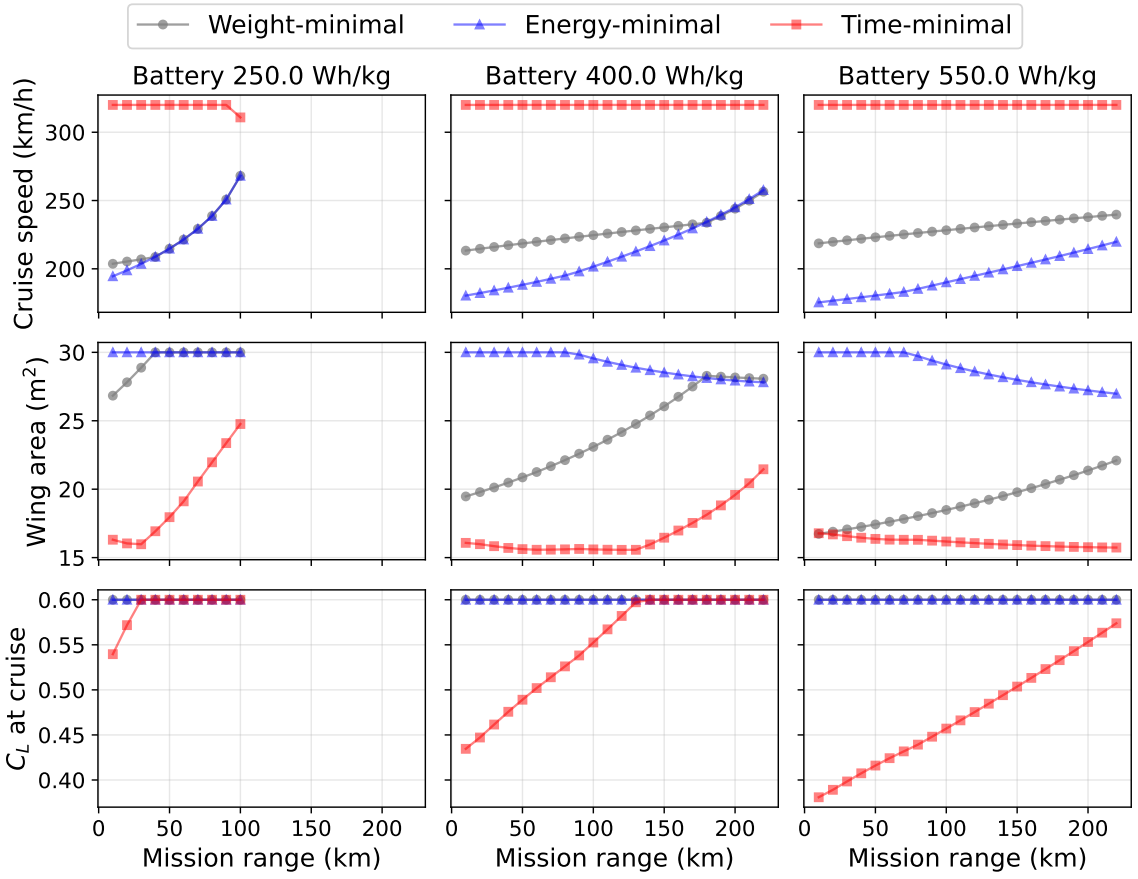


Figure 10 – Optimal parameters versus mission range under varying battery SE levels.

These trends are further explained by the optimal parameters shown in Fig. 10. TM designs consistently reach the upper cruise speed bound of 320 km h^{-1}, except at the feasibility limit (100 km range, 250 W h kg^{-1} SE) where speed is traded for viability. EM designs generally adopt lower cruise speeds to minimize drag and power, while WM designs fly at intermediate speeds. Regarding wing sizing, EM designs require the largest wing areas to sustain lift at lower speeds, whereas TM designs utilize the smallest wings to reduce drag at high speeds. Furthermore, WM and EM designs consistently operate at the maximum allowable lift coefficient ($C_{L,\text{cruise}} = 0.6$), particularly because they tend to adopt lower cruise speeds; at lower dynamic pressure, using the upper C_L bound avoids requiring a larger wing area (and the associated structural and parasitic drag penalties). In contrast, TM designs reach the upper cruise speed bound, which increases dynamic pressure and reduces the required C_L, so the C_L constraint becomes inactive, especially at high battery SE where takeoff weight is lower.

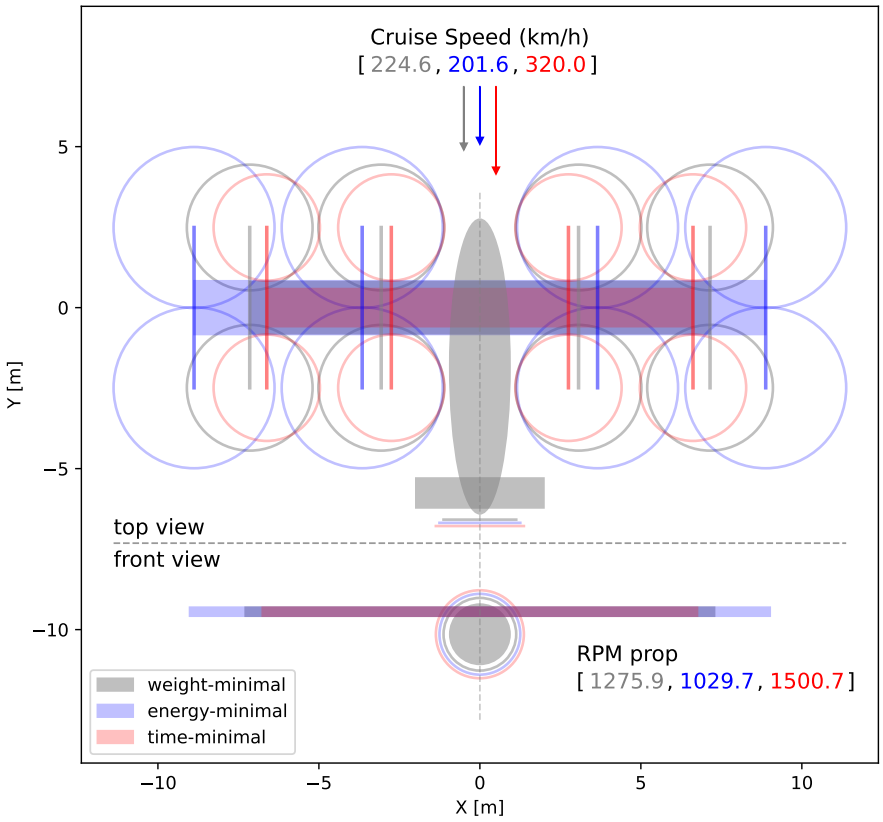


Figure 11 – Optimal geometries for different objectives (Battery SE: 400 W h kg^{-1}, Range: 100 km).

The optimal geometries are visualized in Fig. 11 for a representative case (400 W h kg^{-1} battery SE, 100 km mission range). Despite the nearly overlapping objective trends between the weight- and energy-minimization problems, the resulting geometries differ noticeably. The EM design adopts the largest wing ($S_w \approx 29.6\,\mathrm{m}^2$, $\mathcal{AR}_w \approx 10.7$) to enable a lower cruise speed while satisfying the C_L constraint and reducing induced drags, and it selects the largest lift rotors ($r_{rotor} \approx 2.5\,\mathrm{m}$) to reduce disk loading and hover power. By contrast, the WM design favors a smaller wing ($S_w \approx 23.1\,\mathrm{m}^2$, $\mathcal{AR}_w \approx 8.8$) to reduce structural weight, while maintaining an intermediate cruise speed. The TM design maxes out the cruise speed and consequently selects the smallest wing and lift rotors ($S_w \approx 15.6\,\mathrm{m}^2$, $r_{rotor} \approx 1.65\,\mathrm{m}$); the latter is driven by the spatial clearance constraint, as the small wing limits the available length for rotor spacing. These trade-offs are also reflected in the power and weight breakdowns presented in Figs. 12 and 13, respectively. The EM design consistently achieves the lowest power consumption across all flight segments, resulting in the lowest required energy and battery weight. The WM design achieves the lowest empty weight (structure, propulsion, and equipment). The TM design, prioritizing speed, incurs the highest power and energy consumption, necessitating the heaviest battery and propulsion system, which drives up the total takeoff weight.

Finally, the results of the second study are mapped in Fig. 14. The optimal takeoff weight is shown on a mission requirement map where mission range and cruise speed are fixed inputs, and the optimizer finds the minimum feasible $W_{takeoff}$ for each range-speed pair. The hatched regions indicate infeasible missions (no design satisfying the constraints and bounds). Infeasibility at low speeds ($< 180\,\mathrm{km\,h}^{-1}$) is driven by the stall-margin constraint ($C_{L,cruise} \leq 0.6$): at low dynamic pressure, the wing area reaches its upper bound yet still cannot meet the C_L limit. Infeasibility at long ranges is driven by the MTOW cap (5700 kg), as increasing required energy leads to cascading battery and takeoff weight growth. The red box marks the neighborhood of the Uber Air reference mission requirement [31, 32], centered at 96.6 km range and 241.4 km h^{-1} speed. Increasing battery SE significantly expands the feasible design space; the region around this reference mission is barely feasible at 250 W h kg^{-1} but becomes comfortably feasible at higher SE levels. The takeoff-weight contours exhibit a low-weight "valley": for

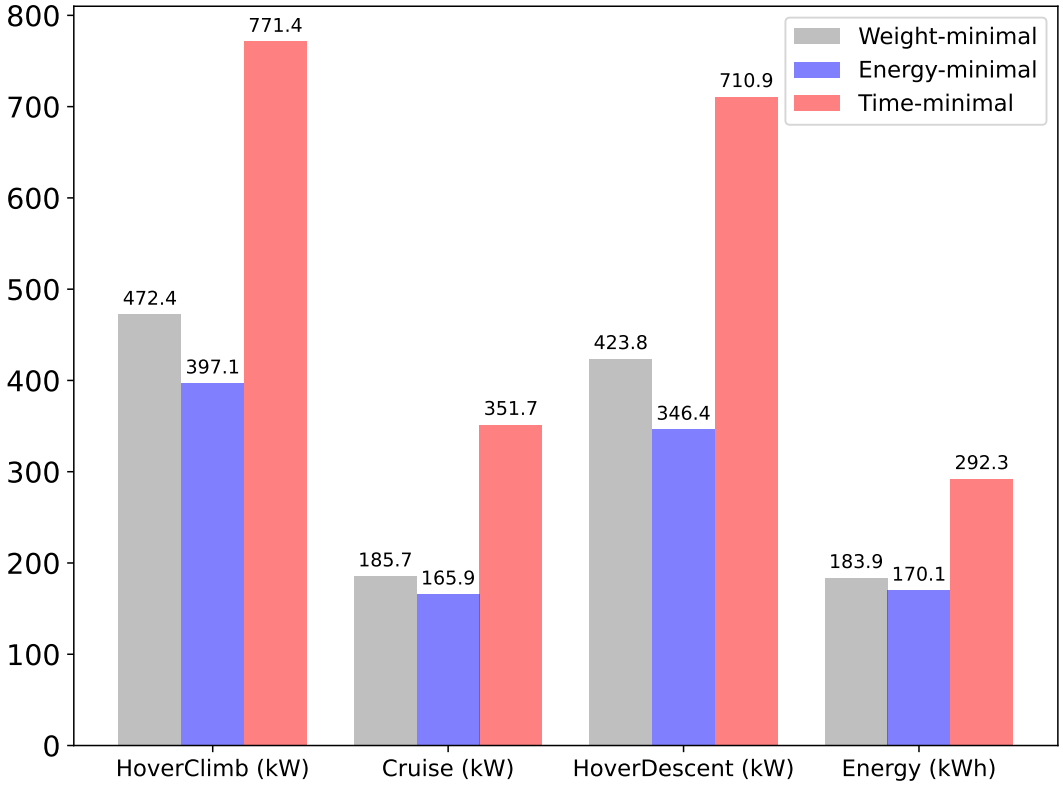


Figure 12 – Segment power and energy breakdown (Battery SE: 400 W h kg^{-1}, Range: 100 km).

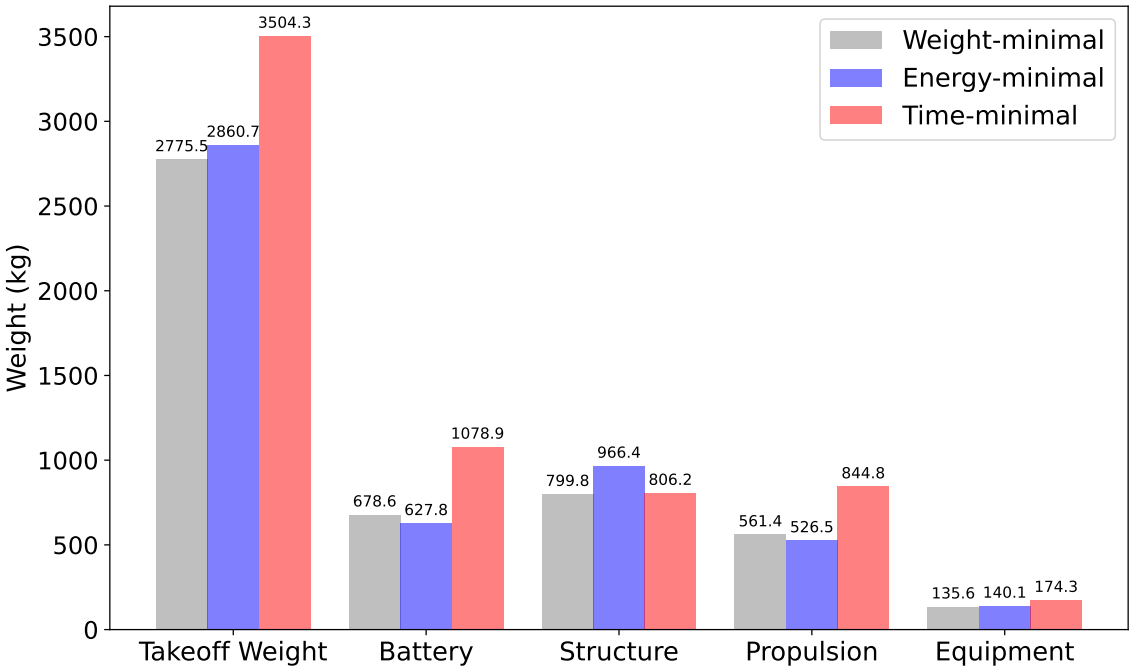


Figure 13 – Component weight breakdown (Battery SE: 400 W h kg^{-1}, Range: 100 km).

a given range, W_{takeoff} is minimized at an intermediate cruise speed and increases toward both lower and higher speeds. At low speeds, reduced dynamic pressure raises the required C_L, pushing the design toward larger wings and eventually activating the C_L constraint (and the wing area upper bound). At high speeds, increasing parasite drag drives higher cruise power and required energy, which in turn increases battery and propulsion weight, raising W_{takeoff}. This valley follows the red-dashed line obtained from the first study where cruise speed was a variable.

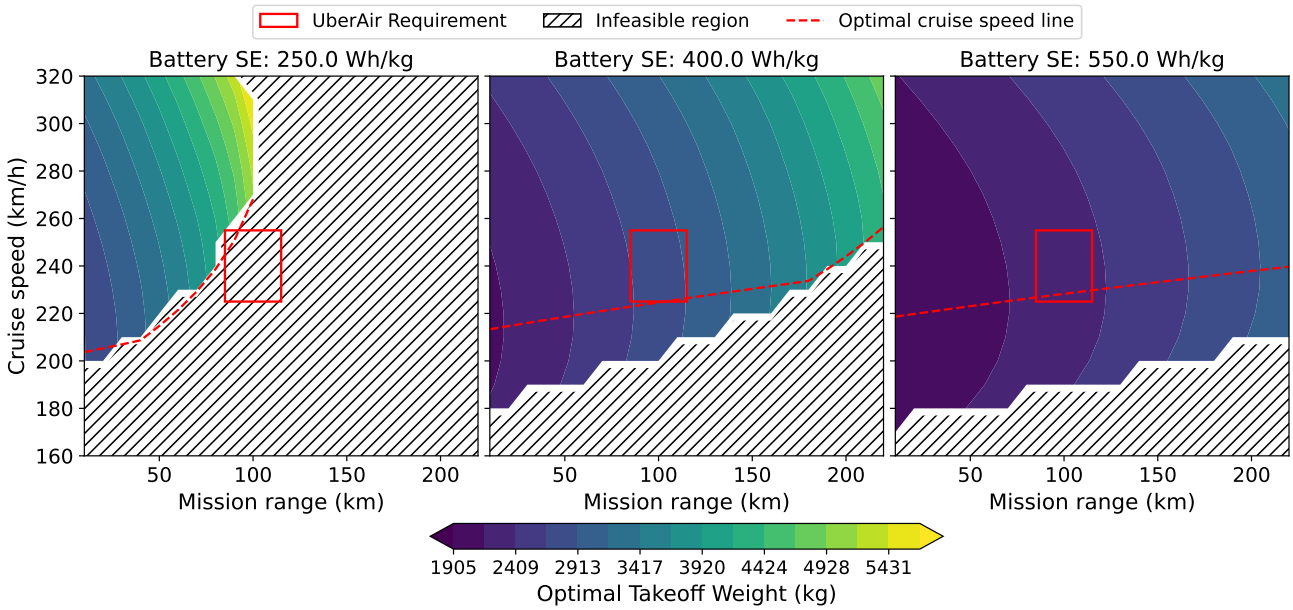


Figure 14 – Weight-based optimization results mapped on the mission requirement space.

3.2 Sensitivity to Projected Technology Levels

The preceding parameter-sweep studies varied a limited number of quantities at a time, such as mission range, cruise speed, or battery SE. Although these sweeps are useful for revealing direct design trends, they do not address the broader question considered here: when multiple technology levels vary simultaneously, which ones account for most of the variation in the resulting optimal eVTOL design? This question is particularly important because the aircraft is re-optimized for each future technology state. Thus, the observed response is not merely the performance change of a fixed design, but the movement of the optimal design itself as the technology vector evolves. To address this question, we used a variance-based global sensitivity analysis (GSA) by utilizing Sobol' indices [49]. For each evaluation year, the conservative and aggressive technology projections shown in Figs. 1–3 define a year-specific projection envelope for the technology variables. The GSA then decomposes the variance of optimal design outputs into contributions from individual variables and their interactions. In practical terms, the analysis asks: if optimal eVTOL designs vary across the projected technology combinations for a given year, how much of that variation is attributable to battery SE, motor SP, converter SP, motor efficiency, converter efficiency, and their coupled effects?

For each evaluation year, the mapping being analyzed is $\Theta(t) \mapsto \mathbf{x}^*(\Theta) \mapsto Y_j(\Theta, \mathbf{x}^*)$, where $\Theta(t) = [\rho_b, \rho_m, \rho_c, \eta_m, \eta_c]$ is the technology vector at year t, $\mathbf{x}^*$ is the optimal design obtained from the Hybrid MDO problem in Table 3, and Y_j is one scalar output of interest. The mission requirements were fixed to the Uber Air reference mission [31, 32] so that the resulting sensitivities isolate the effect of technology maturation rather than changes in mission requirement. For each $t \in \{2030, 2040, 2050, 2060, 2070\}$, the five technology variables in Θ were assumed to vary independently and uniformly within their corresponding annual projection envelopes. Each year was treated as a separate GSA problem; the year itself was not sampled as an uncertain input. This formulation allows the sensitivity structure to be compared across time as the projection envelopes widen and the S-curves of the technology projections approach saturation.

It should be emphasized that the technology variables are not treated here as random variables in a physical sense. Rather, the uniform distributions are assumed over the bounded projection intervals for each year. Therefore, the Sobol' indices are interpreted as sensitivity measures with respect to an assumed probability measure over the prescribed technology space, rather than as probabilistic statements about physical uncertainty. This interpretation is appropriate for the present

study because the goal is to rank dominant technology drivers, rather than to assign probabilities to future technology realizations. Sobol' indices were selected because they provide normalized first- and total-order effects for nonlinear coupled responses, whereas local derivatives or one-at-a-time sweeps cannot capture interactions [50, 51], and screening methods such as Morris [52] do not provide a detailed variance-decomposition attribution.

The Sobol' method decomposes the variance of a scalar output into contributions from each uncertain input and from their interactions. For independent inputs $X_1, \ldots, X_D$ and scalar output Y, the total variance can be written as

$$\mathrm{Var}(Y) = \sum_i V_i + \sum_{i<j} V_{ij} + \sum_{i<j<k} V_{ijk} + \cdots, \tag{15}$$

where V_i represents the variance contribution associated with varying X_i alone, V_{ij} represents the additional contribution arising from the interaction between X_i and X_j, and higher-order terms represent interactions among three or more inputs. Normalizing each variance contribution by the total output variance gives the corresponding Sobol' indices, for example $S_i = V_i/\mathrm{Var}(Y)$ and $S_{ij} = V_{ij}/\mathrm{Var}(Y)$. When all main-effect and interaction terms are included, these normalized contributions sum to unity:

$$\sum_i S_i + \sum_{i<j} S_{ij} + \sum_{i<j<k} S_{ijk} + \cdots = 1. \tag{16}$$

The first-order Sobol' index is the fraction of output variance explained by the main effect of X_i alone:

$$S_{1,i} \equiv S_i = \frac{V_i}{\mathrm{Var}(Y)} = \frac{\mathrm{Var}_{X_i}\left(\mathrm{E}_{\mathbf{x}_{\sim i}}[Y \mid X_i]\right)}{\mathrm{Var}(Y)}. \tag{17}$$

The total-order Sobol' index measures the contribution of X_i and all interaction terms involving X_i:

$$S_{T,i} = \frac{V_i + \sum_{j\neq i} V_{ij} + \sum_{\substack{j<k \\ j,k\neq i}} V_{ijk} + \cdots}{\mathrm{Var}(Y)} = 1 - \frac{\mathrm{Var}_{\mathbf{x}_{\sim i}}\left(\mathrm{E}_{X_i}[Y \mid \mathbf{x}_{\sim i}]\right)}{\mathrm{Var}(Y)}. \tag{18}$$

Thus, $S_{1,i}$ measures the main-effect contribution of X_i, whereas $S_{T,i}$ measures the total involvement of X_i in the output variance. Theoretically, these indices lie between 0 and 1. A value close to 0 means that the input has little influence on the output variance over the prescribed uncertainty range, while a value close to 1 means that the input explains most of the output variance. The first-order indices satisfy $\sum_i S_{1,i} \leq 1$; equality occurs only when the model response is purely additive and there are no interactions. By contrast, $\sum_i S_{T,i}$ can exceed unity because interaction effects are included in the total sensitivity index of every variable participating in the interaction. Consequently, interaction contributions are counted multiple times when the total indices are summed. Therefore, the difference

$$\Delta_i = S_{T,i} - S_{1,i} \tag{19}$$

is interpreted as the portion of the total influence of X_i arising from interactions with other inputs. In other words, if $S_{1,i}$ is close to $S_{T,i}$, the corresponding technology variable primarily affects the output through its direct main effect. If $S_{T,i}$ is substantially larger than $S_{1,i}$, the variable influences the output through interactions with other technology variables. If both indices are close to zero, the variable has negligible influence on that output within the prescribed projection envelope for that year.

The definitions above are integration-based quantities over the full input space. Since the present model includes a nonlinear constrained MDO problem (no closed-form integral), the Sobol' indices were estimated using a sample-based Monte-Carlo-type implementation. Specifically, we used the Saltelli sampling scheme [50], which constructs structured sample matrices that allow the required conditional variance integrals to be estimated from repeated model evaluations. With $D = 5$ technology variables, a base sample size of $n_{\text{base}} = 1024$, and second-order sampling enabled, the number of samples per year is $N = n_{\text{base}}(2D+2) = 12288$. Each sample corresponds to one vector Θ. For every sampled Θ, the full Hybrid MDO problem was solved to minimize W_{takeoff} subject to the given constraints. Consequently, 12 288 weight-based optimizations were executed per evaluation year,

and 61 440 optimizations were executed across the five years, which took around 61.2 min on an Apple M3 Pro. All sampling procedures and Sobol' index calculations were implemented using the SALib framework [53]. The optimized outputs recorded for the GSA were W^*_{takeoff}, W^*_{battery}, $W^*_{\text{propulsion}}$, E^*_{required}, S^*_{w}, $\mathcal{AR}^*_{\text{w}}$, r^*_{rotor}, r^*_{prop}, and Ω^*_{prop}. Here, asterisk means optimized values.

The results of the Sobol' analysis are shown in Figs. 15–17. The quantities plotted are finite-sample estimates of the Sobol' indices defined above; hence, hats are used here to distinguish the numerical estimators from the exact variance-decomposition quantities. For each estimated index, SALib returns a point estimate and a confidence half-width, denoted by c, corresponding to 95 % confidence intervals. Thus, the shaded bands for the first- and total-order indices correspond to

$$\widehat{S}_{1,i} \pm c_{1,i}, \qquad \widehat{S}_{T,i} \pm c_{T,i}, \tag{20}$$

with the lower bounds clipped at zero in the plotted figures. These bands quantify sampling uncertainty in the estimated sensitivity indices due to the finite Saltelli sample size; they should not be interpreted as the physical range of possible aircraft designs or as the conservative–aggressive technology envelope itself. In the frequentist sense, the confidence level describes the long-run reliability of the estimation procedure under repeated sampling, rather than a probability that a particular realized interval contains the exact Sobol' index. For the interaction plots, the displayed quantity is

$$\widehat{\Delta}_i = \widehat{S}_{T,i} - \widehat{S}_{1,i}, \tag{21}$$

which estimates the portion of the total influence of variable i arising through interactions with other technology variables. The corresponding confidence half-width is approximated by

$$c_{\Delta_i} \approx \sqrt{c_{T,i}^2 + c_{1,i}^2}, \tag{22}$$

neglecting covariance between $\widehat{S}_{T,i}$ and $\widehat{S}_{1,i}$. Consequently, a narrow band indicates a stable estimate for the chosen n_{base}, whereas a wide band indicates that the magnitude of that index should be interpreted cautiously. Increasing n_{base} would reduce these estimator uncertainties, but would also increase the number of MDO runs. Small negative estimates, or bands extending slightly outside the theoretical range, can occur due to finite-sample numerical error; in the plotted figures, such negative values are clipped at zero for visualization, while the physical interpretation remains bounded by the Sobol' variance-decomposition framework.

Figure 15 presents the first-order Sobol' indices $\widehat{S}_1$. These results isolate the main-effect contribution of each technology variable. Battery SE dominates the main effects for most outputs throughout the full time horizon. This is particularly clear for W^*_{battery}, where $\widehat{S}_1$ with respect to ρ_{b} remains close to unity across all years, indicating that the optimal battery weight is almost exclusively controlled by battery SE over the projected uncertainty envelope. Similar battery-dominated behavior is observed for other outputs, although the corresponding $\widehat{S}_1$ values gradually decrease toward later years as powertrain specific powers become more influential.

The first-order trends reveal a shift in the main design drivers. For propulsion weight, the main effect of battery SE is high in the near term because battery SE sets the takeoff weight, which in turn sets the thrust and power requirements that size the propulsion system. However, in later years, the main effects of motor and converter SP become comparable to, and eventually larger than, the effect of battery SE. This occurs because propulsion component weights scale as

$$W_{\text{motor}} \propto \frac{1}{\rho_{\text{m}}}, \qquad W_{\text{converter}} \propto \frac{1}{\rho_{\text{c}}}. \tag{23}$$

As the projection envelopes of ρ_{m} and ρ_{c} widen, their main contribution increases substantially.

Figure 16 presents the total-order Sobol' indices $\widehat{S}_T$. Compared with $\widehat{S}_1$, the $\widehat{S}_T$ results include both main and interaction effects. The total-order indices confirm the same overall hierarchy: battery SE is

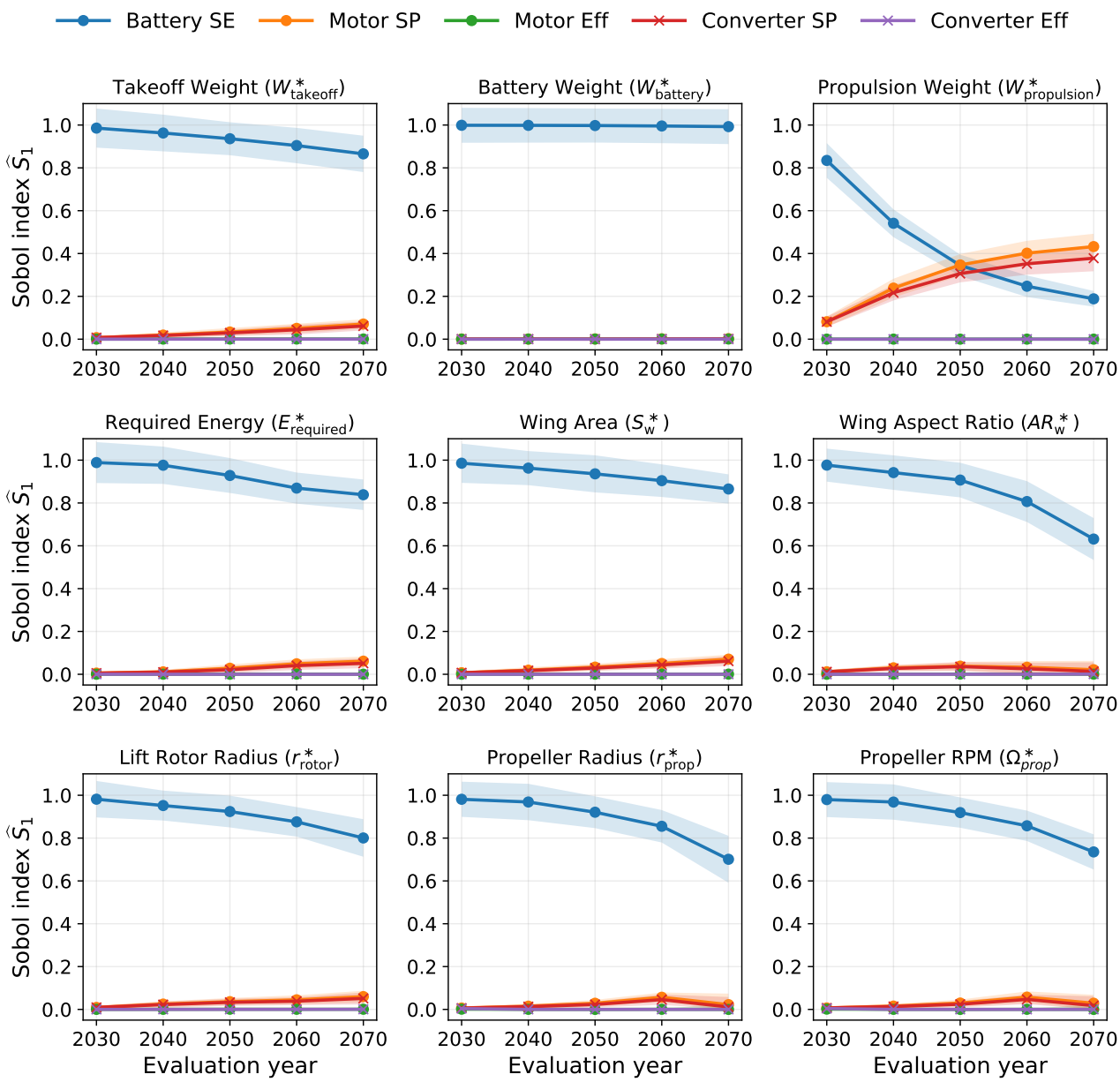


Figure 15 – First-order Sobol' indices ($\widehat{S}_1$) w.r.t. technology variables (Θ) from 2030 to 2070.

the dominant driver of the optimal design ($\widehat{S}_T \approx 0.8 - 1.0$), followed increasingly by motor and converter SP in later years ($\widehat{S}_T \approx 0.1 - 0.4$), while motor and converter efficiencies remain negligible ($\widehat{S}_T \leq 0.1$). The dominance of ρ_{b} is strongest for W^*_{battery}, W^*_{takeoff}, E^*_{required}, S^*_{w}, and r^*_{rotor}. These quantities are closely tied to the weight feedback loop, in which battery SE affects battery weight, battery weight affects takeoff weight, and takeoff weight then affects required thrust, power, energy, and sizing.

A more nuanced trend is observed in the geometry-related outputs. The optimal wing area S^*_{w} follows the behavior of takeoff weight because it is largely governed by the cruise lift constraint. Conversely, the wing aspect ratio $\mathcal{AR}^*_{\text{w}}$ acts as an active aerodynamic-structural trade variable. Increasing $\mathcal{AR}_{\text{w}}$ reduces induced drag, but it also increases structural weight. In the early years, this trade is still primarily driven by battery SE because the vehicle is strongly battery-weight limited. In the later years, however, the widening envelopes for motor and converter SP changes the penalty associated with generating cruise power. As a result, $\mathcal{AR}^*_{\text{w}}$ becomes more sensitive to the powertrain variables. The propeller variables exhibit a similar late-year transition. The optimal propeller radius r^*_{prop} and propeller RPM Ω^*_{prop} are coupled through propeller disk loading, advance ratio, thrust coefficient, and tip Mach number. Their optimal values depend not only on the required thrust and power, but

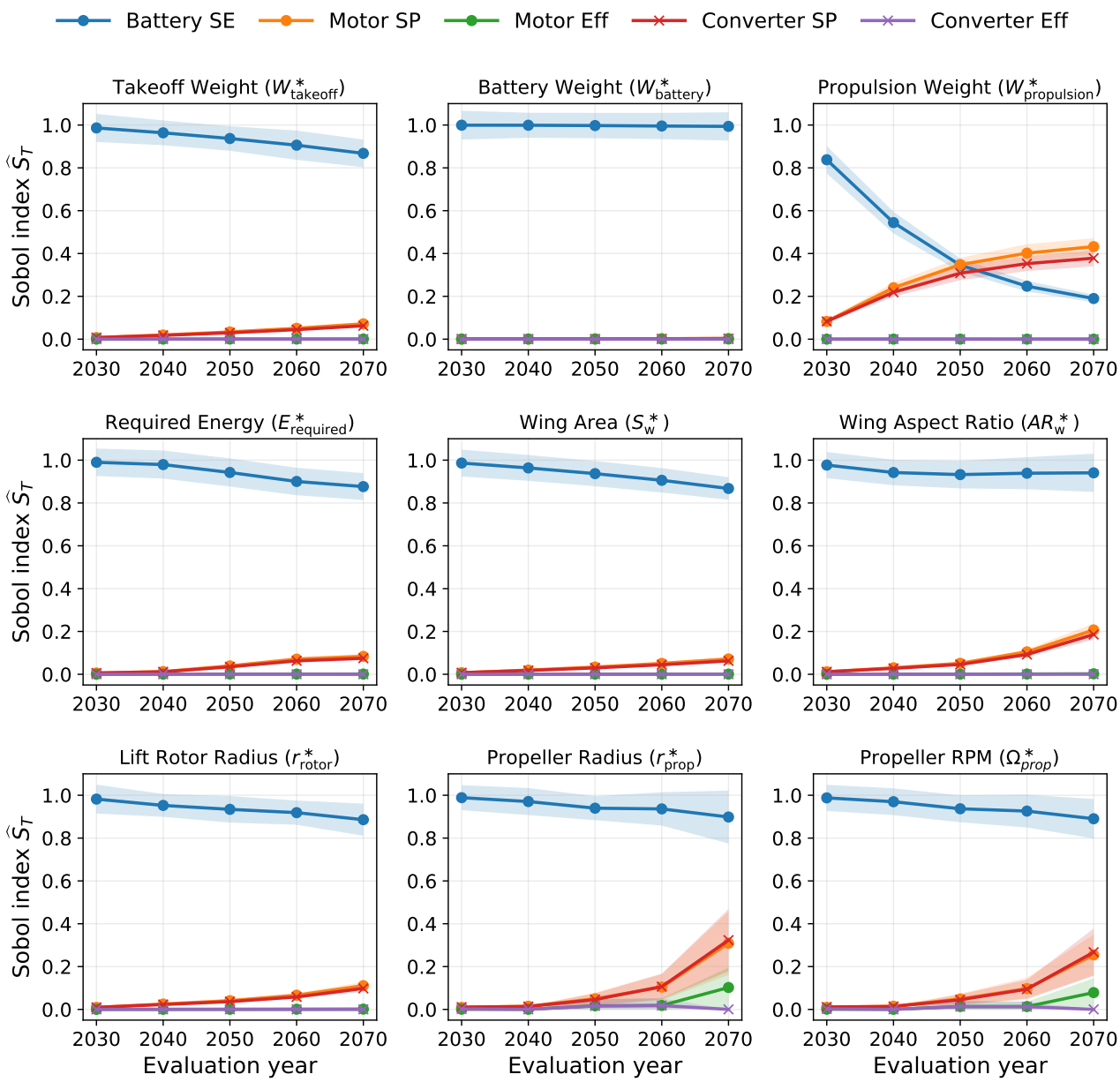


Figure 16 – Total-order Sobol' indices ($\widehat{S}_T$) w.r.t. technology variables (Θ) from 2030 to 2070.

also on how expensive that power is in terms of propulsion weight. Therefore, as the uncertainty in ρ_{m} and ρ_{c} grows, the total-order effects of motor and converter SP on r^*_{prop} and Ω^*_{prop} increase. This indicates that later-year propeller sizing is no longer dictated by battery SE alone, but by the combined battery–propulsion technology state.

To explicitly identify the portion of each total-order effect caused by interactions, Fig. 17 shows $\widehat{S}_T - \widehat{S}_1$. In the early years, the interaction contribution is nearly zero for most outputs, indicating that the response of the optimal design to the technology variables is approximately additive. In this regime, battery SE is the overwhelmingly dominant factor. Toward later years, however, the interaction contribution increases for several geometry-related outputs, most notably $\mathcal{AR}^*_{\text{w}}$, r^*_{prop}, and Ω^*_{prop}. The increase in $\widehat{S}_T - \widehat{S}_1$ for $\mathcal{AR}^*_{\text{w}}$, r^*_{prop}, and Ω^*_{prop} means that the effect of one technology variable increasingly depends on the values of the others. For example, the benefit of a higher wing aspect ratio depends on the takeoff weight, which is strongly affected by ρ_{b}, and also on the propulsion weight penalty associated with the cruise power requirement, which depends on ρ_{m} and ρ_{c}. Similarly, the optimal propeller radius and RPM depend on the coupled balance between required thrust, power, tip-speed constraints, propulsive efficiency, and propulsion weight. These coupled trade-offs become

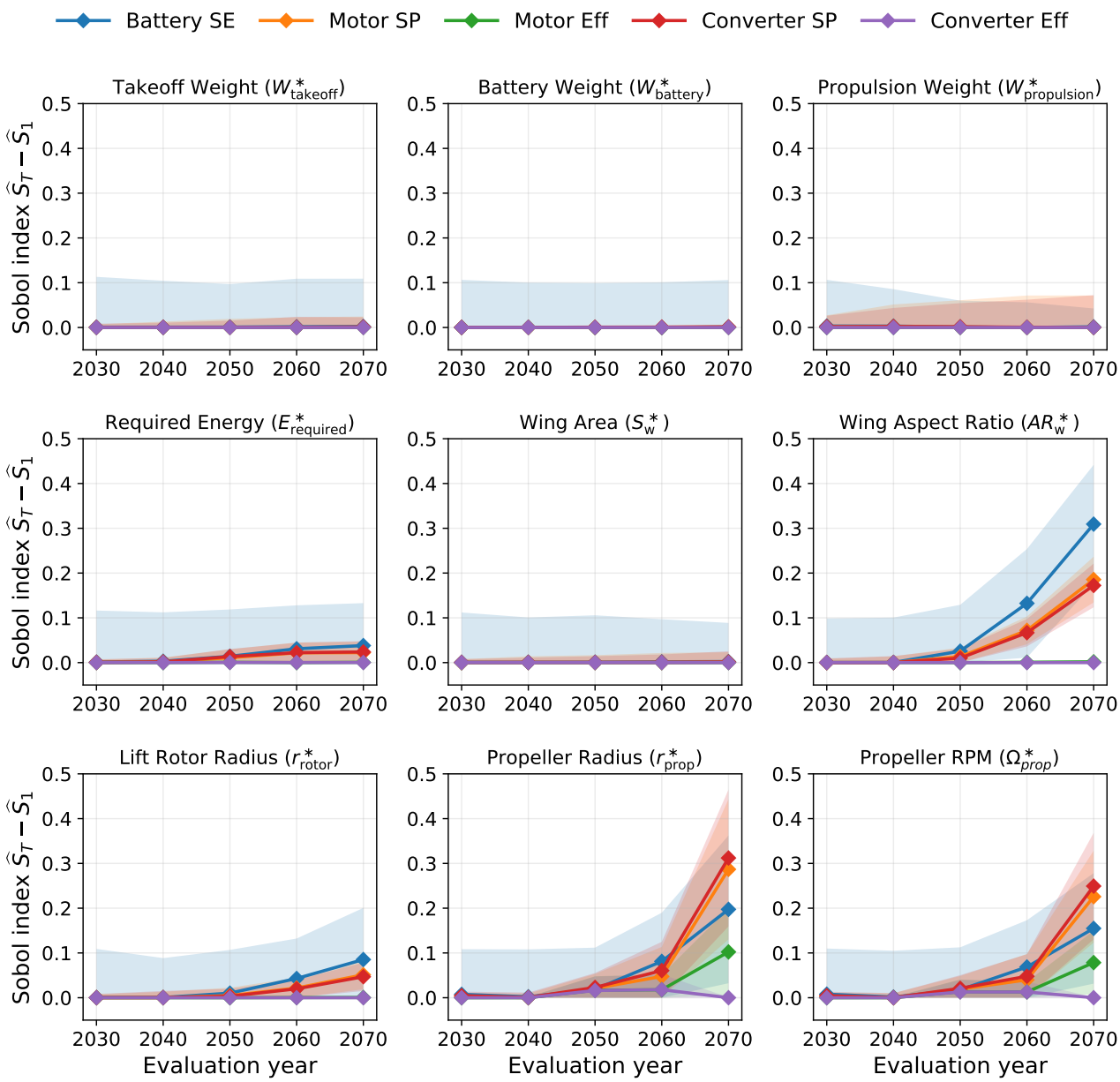


Figure 17 – Total contribution of all interaction terms ($\widehat{S}_T - \widehat{S}_1$) w.r.t. Θ from 2030 to 2070.

more pronounced in later years because the battery and powertrain technology envelopes are simultaneously wide enough to influence the optimal design. The interaction effects for lift rotor radius, wing area, and required energy are weaker. The lift rotor radius is primarily controlled by hover thrust requirement, which remains closely tied to takeoff weight and therefore to battery SE. Wing area is largely constrained by the cruise lift coefficient, so it behaves mainly as a weight-following variable. Required energy inherits some interaction effects through the weight feedback loop, since battery SE, motor SP, and converter SP all influence takeoff weight and thus mission power. Nevertheless, the values of $\widehat{S}_T - \widehat{S}_1$ for these outputs remain small compared with the dominant interaction growth observed for wing aspect ratio and propeller sizing.

Finally, uncertainties in motor and converter efficiencies $(\eta_{\text{m}}, \eta_{\text{c}})$ exert negligible influence on the optimal design variance. Although efficiencies directly affect energy consumption through the system efficiency, their projection envelopes are physically bounded near unity and remain narrow compared with the much wider envelopes associated with battery SE and powertrain SP. Consequently, their Sobol' indices remain negligible across most outputs and years ($\widehat{S}_T - \widehat{S}_1 \leq 0.1$).

4. Future-Aware Optimal Upgrade Strategy

To address technological obsolescence, this section uses the Hybrid MDO formulation selected in Section 2.3 to construct a time-dependent "utopian benchmark" by repeatedly re-optimizing the aircraft under evolving technologies. Guided by the sensitivity results in Section 3.2, the lifecycle technology vector retains battery SE and powertrain specific powers as the dominant drivers, while motor and converter efficiencies are fixed at their SOA values due to their negligible Sobol' indices. We then define a future-aware penalty metric, Ψ, to quantify deviations from the benchmark and formulate a discrete optimization problem to minimize Ψ through optimal *redesign* and *retrofit* schedules.

4.1 Utopian Benchmark and Future-Aware Penalty Metric

To evaluate long-term design and upgrade strategies, we define a time-dependent utopian benchmark representing the best achievable design in each year. Based on the sensitivity results, the technology vector retains the dominant drivers, battery SE and powertrain SPs, while motor and converter efficiencies are fixed at their SOA values because their influence on design variance is negligible:

$$\Theta(t) = [\rho_{\mathrm{b}}(t), \rho_{\mathrm{m}}(t), \rho_{\mathrm{c}}(t), \eta_{\mathrm{m,SOA}}, \eta_{\mathrm{c,SOA}}], \tag{24}$$

where $\eta_{\mathrm{m,SOA}} = 0.96$ and $\eta_{\mathrm{c,SOA}} = 0.98$. For each year, the utopian design $\mathbf{x}^*(t)$ is obtained by optimizing the aircraft under the corresponding technology vector:

$$\mathbf{x}^*(t) = \arg\min_{\mathbf{x}} f(\mathbf{x}, \Theta(t)). \tag{25}$$

Assuming the optimizer reaches the best solution found, $\mathbf{x}^*(t)$ represents the best possible design for year t. The mission is fixed to the Uber Air profile with 600 kg payload, 60 mile range, and 150 mph cruise speed, and the lifecycle spans 2030–2070 with annual time steps. To quantify the suboptimality of a chosen design strategy relative to this ideal baseline, we define a future-aware penalty metric, Ψ. While this metric is generalizable to any objective of interest $f(t)$ (e.g., gross weight or operating cost), this study focuses on the required mission energy, E_{required}. The penalty Ψ is defined as the normalized difference between the time-aggregated objective value of the evaluated strategy, F, and that of the utopian benchmark, $\tilde{F}$.

Let $E_{\mathrm{required}}(\mathbf{x}(t), \Theta(t))$ represent the required mission energy of a design $\mathbf{x}(t)$ when evaluated using the technology level $\Theta(t)$. It is important to note that $\mathbf{x}(t)$ may represent a time-variant design (in the case of a redesign scenario) or a constant vector (in the case of a retrofit scenario). The utopian benchmark energy is denoted as $E_{\mathrm{required}}(\mathbf{x}^*(t), \Theta(t))$. The cumulative performance is defined by the time-aggregated objective functions:

$$F = \int_{2030}^{2070} E_{\mathrm{required}}(\mathbf{x}(t), \Theta(t))\, dt \quad \text{and} \quad \tilde{F} = \int_{2030}^{2070} E_{\mathrm{required}}(\mathbf{x}^*(t), \Theta(t))\, dt. \tag{26}$$

Given the discrete annual time steps ($h = 1$) over the lifespan from $t_0 = 2030$ to $t_N = 2070$ (where $N = 40$), these integrals are approximated using the composite Simpson's 1/3 rule:

$$F \approx \frac{h}{3}\left[E(t_0) + 4\sum_{\substack{i=1 \\ i \text{ odd}}}^{N-1} E(t_i) + 2\sum_{\substack{j=2 \\ j \text{ even}}}^{N-2} E(t_j) + E(t_N)\right], \tag{27}$$

where $E(t_k)$ denotes the required mission energy $E_{\mathrm{required}}(\mathbf{x}(t_k), \Theta(t_k))$ at year k. The utopian aggregate $\tilde{F}$ is computed analogously using the utopian benchmark designs. Consequently, the future-aware penalty metric is defined as:

$$\Psi := \frac{F}{\tilde{F}} - 1. \tag{28}$$

https://doi.org/10.71945/icas2026_0631

A value of $\Psi = 0$ indicates ideal performance matching the utopian benchmark, while a positive value ($\Psi > 0$) quantifies the cumulative degree of suboptimality. This metric serves as the objective function for the upgrade strategy optimization presented in the following subsection.

4.2 Optimal Upgrade Strategy for Redesign and Retrofit Schedules

The utopian benchmark presented previously represents a theoretical limit, assuming the aircraft is continuously redesigned to instantaneously incorporate technological advancements. In practice, however, manufacturers introduce new "blocks" or versions of an aircraft at discrete intervals. Consequently, this section introduces a methodology to determine the optimal scheduling for these discrete upgrades to minimize the lifecycle performance penalty, Ψ.

In this study, an "upgrade" is defined as a major event where the aircraft undergoes significant updates to leverage the latest technology vector, $\Theta(t)$. Two distinct cases are considered:

1. **Clean-Sheet Redesign:** The aircraft is fully redesigned at the upgrade year. The design variables update dynamically, denoted as $\mathbf{x} = \mathbf{x}^*(t)$, alongside the new technology, $\Theta(t)$.
2. **Component-Swap Retrofit:** The airframe remains fixed to the design optimized at the entry-into-service (EIS) year, i.e., $\mathbf{x} = \mathbf{x}^*(t_{\text{EIS}})$. Only the components (battery, motors, and converters) are replaced with the latest technology, $\Theta(t)$.

The objective is to identify a set of discrete time points for these upgrades that minimizes the penalty metric Ψ. This transforms the problem into a discrete optimization task where the design variables are the specific years in which upgrades occur. For this analysis, we assume an aircraft enters service in $t_0 = 2030$ and is retired in $t_4 = 2070$. The aircraft undergoes three intermediate upgrades over this 40-year lifespan, resulting in five distinct operational blocks. The task is to identify the optimal scheduling for the intermediate years $\{t_1, t_2, t_3\}$.

To evaluate a candidate schedule, the total aggregated energy, F_{upgrade}, is computed. Since the time intervals between upgrades, $\Delta t_k = t_{k+1} - t_k$, are variable and non-uniform, the composite Simpson's rule is unsuitable. Furthermore, the discrete upgrade strategy effectively functions as a step function where performance improves at the upgrade year and remains constant until the next block. To account for this, the energy integration is performed using the composite trapezoidal rule:

$$F_{\text{upgrade}}(t_1, t_2, t_3) = \sum_{k=0}^{3} \frac{E(\mathbf{x}, \Theta(t_k)) + E(\mathbf{x}, \Theta(t_{k+1}))}{2}(t_{k+1} - t_k), \tag{29}$$

where the set of upgrade years is $t_k \in \{t_0, t_1, t_2, t_3, t_4\}$. In the redesign case, E is evaluated using $\mathbf{x}^*(t_k)$, whereas in the retrofit case, E is evaluated using the fixed $\mathbf{x}^*(t_0)$. The penalty metric is derived by normalizing this aggregated energy against the utopian benchmark energy, $\tilde{F}$:

$$\Psi(t_1, t_2, t_3) = \frac{F_{\text{upgrade}}(t_1, t_2, t_3)}{\tilde{F}} - 1. \tag{30}$$

The discrete optimization problem is formally stated as:

$$\begin{aligned} \underset{t_1, t_2, t_3}{\text{minimize}} \quad & \Psi(t_1, t_2, t_3) \\ \text{subject to} \quad & t_2 - t_1 > 0, \\ & t_3 - t_2 > 0, \\ & 2031 \leq t_1, t_2, t_3 \leq 2069, \\ & t_1, t_2, t_3 \in \mathbb{Z}. \end{aligned} \tag{31}$$

This problem was solved using a Genetic Algorithm (GA), specifically the NSGA-II algorithm [54] implemented via the pymoo library [55]. The performance of the optimal schedule was compared against a baseline uniform strategy with 10-year intervals ($[2030, 2040, 2050, 2060, 2070]$) across three technology projection scenarios: conservative, nominal, and aggressive.

4.3 Results and Discussion: Redesign and Retrofit Strategies

The results for the clean-sheet redesign and component-swap retrofit cases are illustrated in Figs. 18 and 19, respectively. In the redesign case, the utopian benchmark (black line) illustrates decreasing energy requirements over time as technology improves and the design $\mathbf{x}^*(t)$ is continuously re-optimized. In the retrofit case, the continuous retrofit curve (grey line) demonstrates that while replacing components reduces the required mission energy over time, it remains higher than the utopian benchmark. This gap quantifies the suboptimality of maintaining a fixed airframe design $\mathbf{x}^*(t_{\text{EIS}})$, which is also captured by the future-aware penalty metric Ψ.

The optimal discrete schedules identified by the GA for both strategies are summarized in Table 4. The percentage improvement over the uniform schedule is defined as

$$\Delta_\Psi = \frac{\Psi_{\text{uniform}} - \Psi_{\text{optimal}}}{\Psi_{\text{uniform}}} \times 100\%. \tag{32}$$

Since Ψ measures excess cumulative energy relative to the utopian benchmark, Δ_Ψ represents the relative reduction of this excess penalty, rather than a direct reduction in total energy consumption. In all projection scenarios, the optimal schedules yield lower Ψ values compared to the uniform schedules, suggesting the efficacy of strategic timing. The improvement is more pronounced for redesign, with $\Delta_\Psi = 18.0\,\%$ to $22.0\,\%$, because both the airframe and component technologies are updated at each upgrade year. By contrast, retrofit improvements are only $\Delta_\Psi = 1.2\,\%$ to $2.9\,\%$, because the EIS airframe is retained and much of the penalty relative to the utopian benchmark is therefore irreducible by timing alone. Thus, the retrofit percentages are small relative to redesign, but they still indicate a measurable reduction in the avoidable scheduling penalty.

A key insight derived from both redesign and retrofit analyses is that the optimal upgrade strategy is consistently non-uniform. Regardless of the technology projection scenario, the optimizer clusters upgrades closer together during the earlier years, with intervals of approximately 5–8 years, and spaces them further apart in later years, with intervals of approximately 10–18 years. This behavior aligns with the technology S-curve; the strategy capitalizes on the steepest portion of the curve where technological advancement is most rapid. Conversely, as technology maturation plateaus in later decades, the marginal benefit of frequent upgrades diminishes. Thus, aligning the upgrade schedule with the rate of technological evolution minimizes the lifecycle penalty Ψ more effectively than a uniform approach.

Table 4 – Optimal discrete redesign and retrofit schedules across three projection scenarios.

Strategy	**Scenario**	**Optimal Schedule**	■optimal	■uniform	■ [%]
Redesign	Conservative	[2030, 2035, 2043, 2054, 2070]	0.0794	0.1016	21.9
Redesign	Nominal	[2030, 2036, 2043, 2054, 2070]	0.0365	0.0445	18.0
Redesign	Aggressive	[2030, 2035, 2042, 2052, 2070]	0.0270	0.0346	22.0
Retrofit	Conservative	[2030, 2036, 2044, 2055, 2070]	0.3612	0.3656	1.2
Retrofit	Nominal	[2030, 2036, 2044, 2054, 2070]	0.1517	0.1547	1.9
Retrofit	Aggressive	[2030, 2035, 2042, 2053, 2070]	0.1123	0.1156	2.9

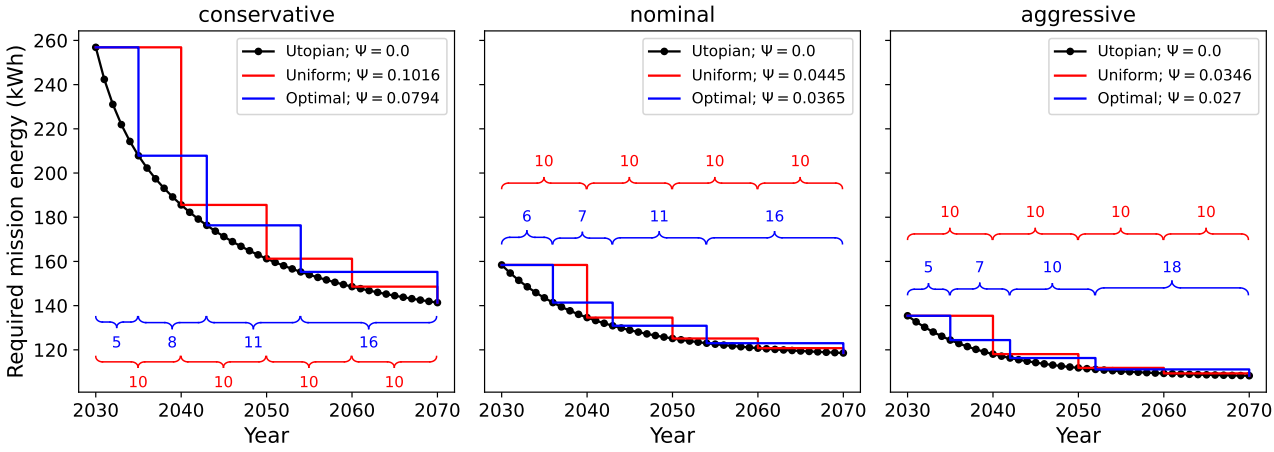


Figure 18 – Optimal discrete redesign schedules across three technology projection scenarios.

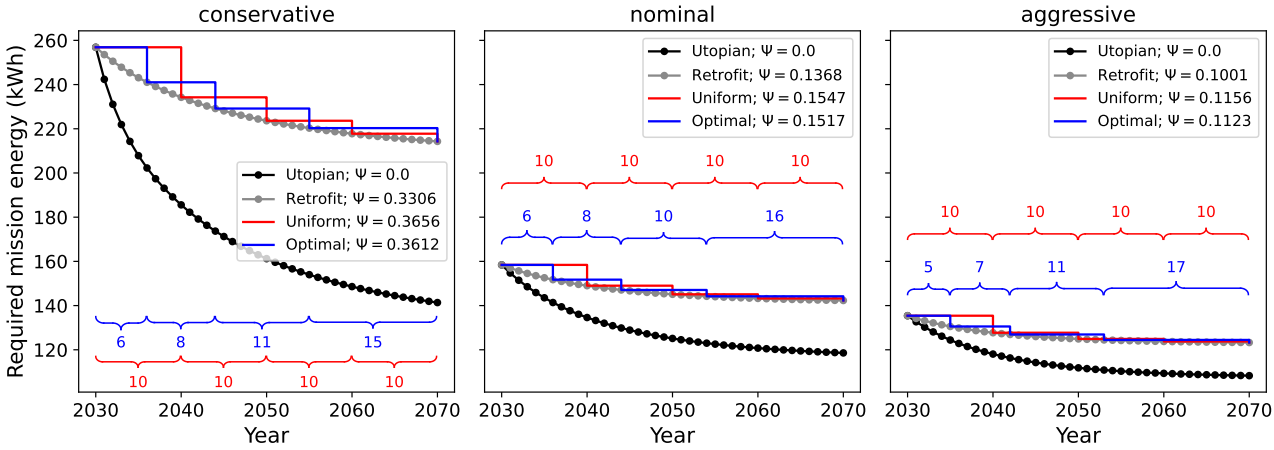


Figure 19 – Optimal discrete retrofit schedules across three technology projection scenarios.

5. Conclusion and Future Work

This study couples MDO with time-dependent technology projections to support future-aware conceptual design of an LPC eVTOL aircraft. Three MDO architectures were benchmarked. The Hybrid MDF–IDF architecture was selected because it offered the best balance of efficiency, robustness, and solution quality: it required only a mean of 15 MDA calls, compared with 282 for MDF and 21 for IDF; all three architectures achieved a 100 % global success rate; and Hybrid produced the non-tied best solution in 392 of the 550 commonly feasible cases, compared with 98 for MDF and 38 for IDF.

The parameter sweeps show that optimal configurations are strongly affected by design objective, mission range, cruise speed, and battery SE. Weight- and energy-minimal designs are closely coupled because reducing takeoff weight also reduces the power and energy required. However, their geometries still differ: energy-minimal designs favor larger wings and lift rotors to reduce cruise and hover power, whereas weight-minimal designs prioritize lower structural and propulsion-system weight. Time-minimal designs, by contrast, operate at the upper cruise speed bound and incur substantial weight and energy penalties. The feasible mission space expands significantly with increasing battery SE, indicating that battery technology remains a primary driver of near-term eVTOL feasibility. The Sobol' GSA further shows that battery SE is the dominant technology driver of the optimized designs, with $\widehat{S}_T \approx 0.8 - 1.0$ for many key outputs. Motor and converter SPs become increasingly influential in later years, with $\widehat{S}_T \approx 0.1 - 0.4$, especially for propulsion weight and selected geometry variables. In contrast, motor and converter efficiencies remain negligible, with $\widehat{S}_T \leq 0.1$, because their projection envelopes are narrow and physically bounded near unity. These results justify retaining battery SE and powertrain SPs as the main time-varying technology drivers in the lifecycle analysis.

Finally, a future-aware penalty metric, Ψ, was introduced to evaluate discrete upgrade schedules relative to a continuously re-optimized utopian benchmark. The optimized schedules are consistently non-uniform, with early upgrade intervals of approximately 5–8 years and later intervals of approximately 10–18 years. Compared with uniform 10-year schedules, these non-uniform schedules reduce Ψ by 18 % to 22 % for clean-sheet redesigns and by 1.2 % to 2.9 % for component-swap retrofits. This indicates that upgrades should be concentrated during rapid technology maturation and spaced farther apart as the technology projections plateau.

Future work should optimize fixed-airframe designs directly against Ψ, allowing initial performance to be traded for long-term adaptability. Robust design selection should also be performed across the three technology scenarios to reduce dependence on a single forecast. Lastly, the framework should use higher-fidelity models, e.g., equivalent circuit and thermal battery models [13, 14] and motor efficiency maps for sizing [11]. Furthermore, cell-aging models [13] would allow the upgrade strategy to be based on actual state-of-health decay rather than purely theoretical technology availability.

6. Acknowledgments

The first and second authors acknowledge financial support from the Hong Kong PhD Fellowship Scheme (HKPFS), administered by the Research Grants Council (RGC) of the University Grants Committee (UGC) of the Hong Kong Special Administrative Region, China.

7. Contact Author Email Address

Contact the first author for further information: alfiyandyhariansyah@gmail.com.

8. Copyright Statement

The authors confirm that they, and/or their company or organization, hold copyright on all of the original material included in this paper. The authors also confirm that they have obtained permission, from the copyright holder of any third party material included in this paper, to publish it as part of their paper. The authors confirm that they give permission, or have obtained permission from the copyright holder of this paper, for the publication and distribution of this paper as part of the ICAS proceedings or as individual off-prints from the proceedings.

References

[1] Garrow LA, German BJ and Leonard CE. Urban air mobility: a comprehensive review and comparative analysis with autonomous and electric ground transportation for informing future research. *Transportation Research Part C: Emerging Technologies*, Vol. 132, 103377, 2021.

[2] Kim HD, Perry AT and Ansell PJ. A review of distributed electric propulsion concepts for air vehicle technology. *Proc 2018 AIAA/IEEE Electric Aircraft Technologies Symposium*, Cincinnati, Ohio, 2018.

[3] Moore MD and Fredericks B. Misconceptions of electric aircraft and their emerging aviation markets. *Proc 52nd Aerospace Sciences Meeting*, National Harbor, Maryland, 2014.

[4] Chen S, Guo Z and Liu D. Impact of propeller arrangement on aerodynamic performance for a high-lift distributed propulsion system. *Engineering Applications of Computational Fluid Mechanics*, Vol. 19, No. 1, 2505701, 2025.

[5] Minervino M, Andreutti G, Russo L and Tognaccini R. Drag reduction by wingtip-mounted propellers in distributed propulsion configurations. *Fluids*, Vol. 7, No. 7, 212, 2022.

[6] Courtin C and Hansman RJ. Safety considerations in emerging electric aircraft architectures. *Proc 2018 Aviation Technology, Integration, and Operations Conference*, Atlanta, Georgia, 2018.

[7] Cao W, Zhang J and Li H. Batteries with high theoretical energy densities. *Energy Storage Materials*, Vol. 26, pp 46-55, 2020.

[8] Khan FMNU, Rasul MG, Sayem ASM and Mandal N. Maximizing energy density of lithium-ion batteries for electric vehicles: a critical review. *Energy Reports*, Vol. 9, pp 11-21, 2023.

[9] Hascaryo RW and Merret JM. Configuration-independent initial sizing method for UAM/eVTOL vehicles. *Proc AIAA AVIATION 2020 FORUM*, Virtual Event, 2020.

[10] Ugwueze O, Statheros T, Horri N, Bromfield MA and Simo J. An efficient and robust sizing method for eVTOL aircraft configurations in conceptual design. *Aerospace*, Vol. 10, No. 3, 311, 2023.

[11] Sarojini D, Ruh ML, Joshy AJ, Yan J, Ivanov AK, Scotzniovsky L, Fletcher AH, Orndorff NC, Sperry M, Gandarillas VE, Asher I, Chambers JT, Gill H, Lee S, Cheng Z, Rodriguez G, Zhao S, Mi C, Nascenzi T, Cuatt T, Winter TF, Guibert AT, Cronk A, Kim HA, Meng S and Hwang JT. Large-scale multidisciplinary design optimization of an eVTOL aircraft using comprehensive analysis. *Proc AIAA SCITECH 2023 Forum*, National Harbor, MD & Online, 2023.

[12] Ruh ML, Fletcher A, Sarojini D, Sperry M, Yan J, Scotzniovsky L, Van Schie SP, Warner M, Orndorff NC, Xiang R, Joshy AJ, Zhao H, Krokowski J, Gill H, Lee S, Cheng Z, Cao Z, Mi C, Silva C, Wolfe L, Chen JS and Hwang JT. Large-scale multidisciplinary design optimization of a NASA air taxi concept using a comprehensive physics-based system model. *Proc AIAA SCITECH 2024 Forum*, Orlando, FL, 2024.

[13] Clarke M and Alonso JJ. Lithium-ion battery modeling for aerospace applications. *Journal of Aircraft*, Vol. 58, No. 6, pp 1323-1335, 2021.

[14] Park J, Jeong T and Yee K. Refined air-cooled battery sizing process for conceptual design of eVTOL aircraft. *Applied Energy*, Vol. 377, 124567, 2025.

[15] Bacchini A and Cestino E. Electric VTOL configurations comparison. *Aerospace*, Vol. 6, No. 3, 26, 2019.

[16] Kadhiresan AR and Duffy MJ. Conceptual design and mission analysis for eVTOL urban air mobility flight vehicle configurations. *Proc AIAA Aviation 2019 Forum*, Dallas, Texas, 2019.

[17] Johnson W and Silva C. NASA concept vehicles and the engineering of advanced air mobility aircraft. *The Aeronautical Journal*, Vol. 126, No. 1295, pp 59-91, 2022.

[18] Duffy M, Sevier AE, Hupp R, Perdomo E and Wakayama S. Propulsion scaling methods in the era of electric flight. *Proc 2018 AIAA/IEEE Electric Aircraft Technologies Symposium*, Cincinnati, Ohio, 2018.

[19] Smart JT and Alonso JJ. Primary weight estimation for eVTOLs via explicit analysis and surrogate regression. *Proc AIAA Aviation 2019 Forum*, Dallas, Texas, 2019.

[20] Johnson W. NDARC - NASA design and analysis of rotorcraft. Technical Report NASA/TP-20220000355/APPX-A, NASA Ames Research Center, Moffett Field, CA, 2023.

[21] Vegh JM, Botero E, Clarke M, Smart J and Alonso J. Current capabilities and challenges of NDARC and SUAVE for eVTOL aircraft design and analysis. *Proc AIAA Propulsion and Energy 2019 Forum*, Indianapolis, IN, 2019.

[22] Chauhan SS and Martins JRRA. Tilt-wing eVTOL takeoff trajectory optimization. *Journal of Aircraft*, Vol. 57, No. 1, pp 93-112, 2020.

[23] Kaneko S and Martins JRRA. Simultaneous optimization of design and takeoff trajectory for an eVTOL aircraft. *Aerospace Science and Technology*, Vol. 155, 109617, 2024.

[24] Reyner C and Liem RP. Energy-efficient trochoidal path planning for unmanned aircraft under wind and performance constraints. *Drones*, Vol. 10, No. 6, 426, 2026.

[25] Chakraborty I and Mishra AA. Sizing of tilt-wing aircraft with all-electric and hybrid-electric propulsion. *Journal of Aircraft*, Vol. 60, No. 1, pp 245-264, 2023.

[26] Bhandari R and Chakraborty I. Sizing and optimization of multi eVTOL configuration for urban air mobility applications. *Proc AIAA SCITECH 2025 Forum*, Orlando, FL, 2025.

[27] Reyner C, Lee C, Kim D and Liem RP. Mission-based optimal propeller selection for VTOL SUAV configuration. *Proc 34th Congress of the International Council of the Aeronautical Sciences*, Florence, Italy, 2024.

[28] Tiede B, O'Meara C and Jansen R. Battery key performance projections based on historical trends and chemistries. *Proc 2022 IEEE Transportation Electrification Conference & Expo (ITEC)*, Anaheim, CA, USA, pp 754-759, 2022.

[29] Pastra CL, Hall C, Cinar G, Gladin J and Mavris DN. Specific power and efficiency projections of electric machines and circuit protection exploration for aircraft applications. *Proc 2022 IEEE Transportation Electrification Conference & Expo (ITEC)*, Anaheim, CA, USA, pp 766-771, 2022.

[30] Hall C, Pastra CL, Burrell A, Gladin J and Mavris DN. Projecting power converter specific power through 2050 for aerospace applications. *Proc 2022 IEEE Transportation Electrification Conference & Expo (ITEC)*, Anaheim, CA, USA, pp 760-765, 2022.

[31] Holden J and Goel N. Uber Elevate: fast-forwarding to a future of on-demand urban air transportation. 2016.

[32] Uber Elevate. UberAir vehicle requirements and missions. 2019.

[33] Federal Aviation Administration. Minimum fuel requirements for flight in VFR conditions.

[34] McDonald RA and Gloudemans JR. Open vehicle sketch pad: an open source parametric geometry and analysis tool for conceptual aircraft design. *Proc AIAA SCITECH 2022 Forum*, San Diego, CA & Virtual, 2022.

[35] Gray JS, Hwang JT, Martins JRRA, Moore KT and Naylor BA. OpenMDAO: an open-source framework for multidisciplinary design, analysis, and optimization. *Structural and Multidisciplinary Optimization*, Vol. 59, No. 4, pp 1075-1104, 2019.

[36] Martins JRRA and Lambe AB. Multidisciplinary design optimization: a survey of architectures. *AIAA Journal*, Vol. 51, No. 9, pp 2049-2075, 2013.

[37] Lambe AB and Martins JRRA. Extensions to the design structure matrix for the description of multidisciplinary design, analysis, and optimization processes. *Structural and Multidisciplinary Optimization*, Vol. 46, No. 2, pp 273-284, 2012.

[38] Bacchini A, Cestino E, Van Magill B and Verstraete D. Impact of lift propeller drag on the performance of eVTOL lift+cruise aircraft. *Aerospace Science and Technology*, Vol. 109, 106429, 2021.

[39] Raymer DP. *Aircraft design: a conceptual approach*. 5th edition, American Institute of Aeronautics and Astronautics, Reston, VA, 2012.

[40] Leishman G. *Introduction to aerospace flight vehicles*. Embry-Riddle Aeronautical University, 2022.

[41] Prouty RW. *Helicopter performance, stability, and control*. R.E. Krieger Pub. Co, Malabar, FL, 1995.

[42] Leishman JG. *Principles of helicopter aerodynamics*. 2nd edition, Cambridge University Press, Cambridge, 2006.

[43] Johnson W. *Rotorcraft aeromechanics*. Cambridge University Press, Cambridge, 2013.

[44] Govindarajan B and Sridharan A. Conceptual sizing of vertical lift package delivery platforms. *Journal of Aircraft*, Vol. 57, No. 6, pp 1170-1188, 2020.

[45] Zhao S, Guo Z, Yan K, Wan S, He F, Sun B and Wang G. Towards high-energy-density lithium-ion batteries: strategies for developing high-capacity lithium-rich cathode materials. *Energy Storage Materials*, Vol. 34, pp 716-734, 2021.

[46] Menye JS, Camara MB and Dakyo B. Lithium battery degradation and failure mechanisms: a state-of-the-art review. *Energies*, Vol. 18, No. 2, 342, 2025.

[47] Roskam J. *Airplane design part V: component weight estimation*. DARcorporation, Lawrence, Kan, 1986.

[48] European Union Aviation Safety Agency (EASA). Special condition for small-category VTOL-capable aircraft, issue 2 (SC-VTOL-02). 2024.

[49] Sobol IM. Global sensitivity indices for nonlinear mathematical models and their Monte Carlo estimates. *Mathematics and Computers in Simulation*, Vol. 55, No. 1-3, pp 271-280, 2001.

[50] Saltelli A, Annoni P, Azzini I, Campolongo F, Ratto M and Tarantola S. Variance based sensitivity analysis of model output. Design and estimator for the total sensitivity index. *Computer Physics Communications*, Vol. 181, No. 2, pp 259-270, 2010.

[51] Saltelli A and Annoni P. How to avoid a perfunctory sensitivity analysis. *Environmental Modelling & Software*, Vol. 25, No. 12, pp 1508-1517, 2010.

[52] Morris MD. Factorial sampling plans for preliminary computational experiments. *Technometrics*, Vol. 33, No. 2, pp 161-174, 1991.

[53] Iwanaga T, Usher W and Herman J. Toward SALib 2.0: advancing the accessibility and interpretability of global sensitivity analyses. *Socio-Environmental Systems Modelling*, Vol. 4, 18155, 2022.

[54] Deb K, Pratap A, Agarwal S and Meyarivan T. A fast and elitist multiobjective genetic algorithm: NSGA-II. *IEEE Transactions on Evolutionary Computation*, Vol. 6, No. 2, pp 182-197, 2002.

[55] Blank J and Deb K. Pymoo: multi-objective optimization in Python. *IEEE Access*, Vol. 8, pp 89497-89509, 2020.